PHYSICAL REVIEW E VOLUME 48, NUMBER 4 OCTOBER 1993

Instability and pattern formation in colloidal-suspension Taylor-Couette flow

Jian-Yang Yuan* and David M. Ronis
Department of Chemistry, McGill University, 801 Sherbrooke Street West, Montreal, Quebec, Canada H3A 2K6

(Received 4 March 1993)

A theory of Taylor-Couette flow in colloidal crystals formed from suspensions of highly charged, poorly screened particles is presented. We show that the usual Taylor instability is suppressed and two new types of instability emerge at low shear rates. These can lead to pattern formation and can form vertical striped phases. The results are discussed in light of the experiments of Weitz, Dozier, and Chaikin [J. Phys. (Paris) Colloq. **46**, C3–257 (1985)] and possible light-scattering experiments are analyzed.

PACS number(s): 82.70.Dd, 05.40.+j, 62.20.−x

I. INTRODUCTION

Charged colloidal particles can form crystalline suspensions at very low packing fractions. Poorly screened, electrostatic repulsion between the colloidal particles is the driving force for the crystallization, and the resulting crystals are extremely soft [1]. It is well known that suspended particles can drastically alter the dynamical properties of a fluid, although the effects are usually proportional to the packing fraction of the suspension. The same is true for extremely dilute charged colloidal suspensions, and there have been several experimental and theoretical studies of these systems in simple hydrodynamic flows. Of these, the most relevant for this work are the studies of shear-induced melting phenomena which has been examined experimentally [2,3] and for which several different theories have been proposed [4,5].

Some novel phenomena were observed by Weitz, Dozier, and Chaikin [2] who found that the usual Taylor instability is suppressed when colloidal crystal is placed between corotating cylinders, and instead, the suspension forms a pattern of colored vertical stripes that rotates in time. It is these phenomena that are the subject of this work, and we theoretically investigate Taylor-Couette flows in colloidal suspensions.

When the inner cylinder is rotated, one would expect the Taylor instability to occur when the critical Taylor number is reached [6]. However, in a crystalline colloidal suspension, the resulting Taylor roll would require that the colloidal crystal be strongly deformed. This costs elastic energy, and hence one should naively expect that the critical Taylor number will increase. While this argument is correct for the formation of Taylor rolls, it ignores other instability mechanisms that are specific to sheared crystals.

The behavior of molecular solids under shear is usually analyzed in terms of dislocations, and indeed this was how the experiment of Ref. [2] was analyzed. In molecular solids, instability mechanisms associated with anharmonic aspects of the potential [7] usually require too much energy and hence do not occur in practice. This is not necessarily the case for sheared colloidal crystals since the elastic moduli are so small. Another difference lies in how the shear is transmitted to the crystal; in the colloidal system it is primarily through the motion of the underlying liquid, while it is applied at the surface of the crystal in molecular systems.

For plane Couette flows in three spatial dimensions, it has been shown [4] that the two-dimensional (2D) shearing motion of the colloidal particles in the crystal, which arises when the underlying fluid is laminarly sheared, results in a periodic modulation of the elastic properties of the crystal; this in turn leads to a Mathieu-Hill instability involving *long-wavelength* transverse acoustic modes of the system. While the precise details of motion of the colloidal particles in the 2D sheared phases may be nontrivial (e.g., zigzag motions [3]), all that really matters for the Mathieu-Hill mechanism is that the instantaneous primitive lattice vectors be periodic functions of time. The critical shear rate is strongly dependent on the system size; it is vanishingly small for sufficiently wide systems and lies in the range observed in the experiments when the appropriate physical parameters are used (about 20 Hz in Ref. [3]). Finally, while planar geometry is more difficult to realize experimentally, the pure fluid hydrodynamics has the advantage of being stable.

In this paper, we present a theory for the long-wavelength properties of a sheared colloidal crystal in the Taylor geometry. We will show that the critical Taylor number is increased; nonetheless, we find two instabilities which operate at low shear rates when either the inner or outer cylinder is rotated. Moreover, one of mechanisms involves modes which have many of the geometric features found in the experiments.

In Sec. II we derive continuum equations of motion for a dilute sheared crystalline suspension and underlying fluid in the Taylor geometry, i.e., when the suspension is confined to a region between coaxial cylinders, either of which may be rotated. These equations should be valid for long wavelength motions of the system. They generalize those presented in Ref. [4] and are based on the same physical assumptions. In particular, the colloidal particles are taken to be pointlike and their interaction with the underlying fluid is via a Stokes drag coefficient.

A linear stability analysis of the laminar flow solutions to these equations of motion is performed in Sec. III. While we find axially symmetric Taylor roll instabilities, these are not the first modes to go unstable for reasonable

1063-651X/93/48(4)/2880(18)/$06.00

values of the transverse sound speed of the colloidal crystal. Instead, the system first becomes unstable through one of two mechanisms: the Mathieu-Hill mechanism discussed in Ref. [4] and a mechanism associated with supersonic flow in elastic systems. In either case, the marginal state is uniform along the axis of the cylinders and consists of a large number of uniformly spaced, rotating stripes. This is what is observed in the experiments of Weitz, Dozier, and Chaikin [2].

Nonlinear corrections are considered in Sec. IV; the resulting nonlinear equations are solved numerically, and some comparisons with the results of Weitz, Dozier, and Chaikin [2] are made. Section V contains an analysis of the elastic light-scattering experiment. We show that the Bragg scattering pattern will be distorted by three effects: the rotation of the fluid, the shearing of the lattice due to the presence of a shear gradient in the fluid, and, finally, the distortion of the lattice associated with the instabilities. Finally, Sec. VI contains a summary and discussion.

II. BASIC THEORY AND PRELIMINARY ANALYSIS

As was discussed in Ref. [4], the equations of motion for a colloidal suspension and the underlying fluid can be written as

$$m_c \ddot{\mathbf{r}}_\alpha = -6\pi\eta_f R_c[\dot{\mathbf{r}}_\alpha - \mathbf{v}(\mathbf{r}_\alpha, t)] + \sum_{\beta\,(\neq\alpha)} \mathbf{F}(\mathbf{r}_\alpha - \mathbf{r}_\beta), \tag{2.1}$$

and

$$\rho_f \left[\frac{\partial \mathbf{v}}{\partial t} + \mathbf{v}\cdot\nabla\mathbf{v} \right] = -\nabla p_h(\mathbf{r},t) + \eta_f \nabla^2 \mathbf{v}(\mathbf{r},t) + 6\pi\eta_f R_c \sum_\alpha \delta(\mathbf{r}-\mathbf{r}_\alpha)[\dot{\mathbf{r}}_\alpha - \mathbf{v}(\mathbf{r},t)], \tag{2.2}$$

where ρ_f and η_f are the mass density and the dynamic viscosity of the fluid respectively, p_h is the hydrostatic pressure, R_c is the radius, m_c is the mass of colloid, $\mathbf{F}(\mathbf{r}_\alpha - \mathbf{r}_\beta)$ is the force the βth colloidal particle at position $\mathbf{r}_\beta$ exerts on the αth at $\mathbf{r}_\alpha$, and $\mathbf{v}(\mathbf{r},t)$ is the fluid velocity field.

In this work, we shall focus on the system's behavior when it is sheared at low shear rate. By low shear rate, we mean that $\xi \equiv 6\pi\eta_f R_c \tau_h / m_c$, where τ_h is a characteristic time of the hydrodynamic shear, is sufficiently large. In this event, the colloid particles will approximately follow the surrounding fluid, i.e.,

$$\dot{\mathbf{r}}_\alpha = \mathbf{v}(\mathbf{r}_\alpha, t) + O(\xi^{-1}). \tag{2.3}$$

For typical colloid suspension in water R_c is $O(0.1\ \mu\text{m})$. Hence, if $\tau_h \sim 10^{-2}$ sec, corresponding to a shear rate of about 100 sec^{-1}, one finds $\xi \sim 10^6$. Therefore, treating ξ^{-1} as a small parameter is a good approximation [4].

No-slip boundary conditions are imposed on the fluid at the walls of the system, i.e., the tangential components of the fluid velocity equal the corresponding components of the surface velocity, while the normal component vanishes. With these boundary conditions, it is well known [6] that steady Taylor-Couette flow in cylindrical, (r,ϕ,z), coordinates has $v_r^{(0)} = v_z^{(0)} = 0$, while

$$v_\phi^{(0)} \equiv r\Omega(r) = r \left[\frac{(\Omega_2 R_2^2 - \Omega_1 R_1^2)}{R_2^2 - R_1^2} + \frac{(\Omega_1 - \Omega_2) R_1^2 R_2^2}{(R_2^2 - R_1^2) r^2} \right], \tag{2.4}$$

where Ω_i and R_i are angular velocities and radii of inner $(i=1)$ and outer $(i=2)$ cylinders. In addition, this state is stable as long as the Taylor number is less than the critical one [6].

In the absence of shear, the colloid particles will crystallize if the intercolloid screened electrostatic repulsion energy at the average distance between particles is large with respect to thermal energies. Of course, placing such a crystal into a cylindrical geometry will distort (i.e., bend) the crystal or introduce dislocations. Nonetheless, these effects will be unimportant locally if the radii of the inner and outer cylinders of the Taylor cell are large compared to the crystal lattice spacings, and will not be considered further.

As was shown in Ref. [4], a laminar steady state can arise in plane Couette flow, even in the presence of colloid. In this state, adjacent layers of colloidal particles slide over one another as they follow the fluid streamlines. In curved geometries, the argument used in Ref. [4] is not exact; specifically, the sheared crystal does not necessarily have inversion symmetry, and hence one cannot argue that the intercolloid force terms cancel exactly for laminar states of flow. This will result in a modification of the velocity profile. Nonetheless, there are two reasons why we may neglect this effect: (1) the extra force terms are proportional to the average colloid density which is very small; and (2) the magnitude of the net intercolloid force resulting from breaking local inversion symmetry will be small as long as the range of the intercolloid forces is small compared with the Taylor cell radii. Thus the system should approximately behave as if it were locally planar when the preceding conditions hold. More importantly, the usual Taylor-Couette velocity profile, cf. Eq. (2.4), will still be valid, and our goal is to examine the stability of these laminar states.

In a sheared colloidal crystal, the individual colloidal particles do not remain near fixed lattice positions; rather they follow the rotation of the underlying fluid, and hence the particle displacements need not be small. Nonetheless, a displacement field can be introduced as follows. Let $\mathbf{R}_\alpha(t)$ be the position of the αth particle in the crystal at time t in the laminar flow and introduce a displacement field $\boldsymbol{\eta}(\mathbf{r},t)$ by requiring that

$$\mathbf{r}_\alpha(t) \equiv \mathbf{R}_\alpha(t) + \boldsymbol{\eta}(\mathbf{r}_\alpha(t), t).$$

Strictly speaking, $\eta(\mathbf{r},t)$ is only defined at discrete points in space; this is not a serious limitation as long as we restrict our discussion to cases where $\boldsymbol{\eta}(\mathbf{r},t)$ is characterized by length scales that are large with respect to the lattice constants characterizing the sheared colloidal crystal. Indeed, if this restriction is not valid, as was shown by Felderhof and Jones [8], the equations of motion must be modified to account for the strong relaxation mechanisms associated with counterion plasmons.

In performing a linear stability analysis of the laminar state, we assume that the displacement field $\boldsymbol{\eta}(\mathbf{r},t)$ and the deviation of velocity field from the laminar flow $\delta\mathbf{v}(\mathbf{r},t)$ are small. Hence

$$\mathbf{r}_\alpha(t) \sim \mathbf{R}_\alpha(t) + \boldsymbol{\eta}(\mathbf{R}_\alpha(t),t) + O(\eta^2) \tag{2.5}$$

and

$$\mathbf{v}(\mathbf{r},t) \equiv \mathbf{v}^{(0)}(\mathbf{r}) + \delta\mathbf{v}(\mathbf{r},t). \tag{2.6}$$

The colloid may be treated as a continuum as long as the deviations are characterized by long length scales. In this case, linearizing the equations of motion shows that

$$m_c D_t^2 \boldsymbol{\eta}(\mathbf{r},t) = -6\pi\eta_f R_c [D_t \boldsymbol{\eta}(\mathbf{r},t) - \delta\mathbf{v}(\mathbf{r},t) - \boldsymbol{\eta}(\mathbf{r},t)\cdot\nabla\mathbf{v}(\mathbf{r},t)] + \mathbf{f}(\mathbf{r},t), \tag{2.7}$$

and

$$\begin{aligned} \rho_f[D_t \delta\mathbf{v}(\mathbf{r},t) + \delta\mathbf{v}(\mathbf{r},t)\cdot\nabla\mathbf{v}(\mathbf{r},t)] &= -\nabla\delta p_h(\mathbf{r},t) + \eta_f \nabla^2 \delta\mathbf{v}(\mathbf{r},t) \\ &\quad + 6\pi\eta_f R_c \sum_\alpha \delta(\mathbf{r}-\mathbf{R}_\alpha)[D_t\boldsymbol{\eta}(\mathbf{R}_\alpha,t) - \delta\mathbf{v}(\mathbf{R}_\alpha,t) \\ &\quad - \boldsymbol{\eta}(\mathbf{R}_\alpha,t)\cdot\nabla\mathbf{v}(\mathbf{R}_\alpha,t)]. \end{aligned} \tag{2.8}$$

Here,

$$D_t \equiv \frac{\partial}{\partial t} + \mathbf{v}(\mathbf{r})\cdot\nabla$$

and the superscript (0) for the steady-state velocity field has been dropped.

The force term $\mathbf{f}(\mathbf{r},t)$ arises from the interactions between the colloidal particles and is discussed in Appendix A. It depends on the details of sheared colloid lattice, and we use a variant of the Kramers-Moyal expansion [9] to express the force as a gradient of a stress tensor, i.e.,

$$\mathbf{f}(\mathbf{r},t) = -\nabla\cdot\overleftrightarrow{\sigma}(\mathbf{r},t).$$

In general, the stress tensor is a functional of the strain tensor $\partial\eta^i(\mathbf{r},t)/\partial x^j$. However, only the first derivatives of $\boldsymbol{\eta}(\mathbf{r},t)$ need be considered as long as the range of the intercolloid interactions is small with respect to the length scales characterizing $\boldsymbol{\eta}(\mathbf{r},t)$. To leading order in the ratio of these length scales we find that

$$\overleftrightarrow{\sigma}(\mathbf{r},t) = \tfrac{1}{2} \sum_{\substack{\alpha,\beta \\ (\beta\neq\alpha)}} \mathbf{R}_{\alpha,\beta}(t)\mathbf{F}(\mathbf{R}_{\alpha,\beta}(t) + \mathbf{R}_{\alpha,\beta}(t)\cdot\nabla\boldsymbol{\eta}(\mathbf{r},t)), \tag{2.9}$$

where $\mathbf{R}_{\alpha,\beta}(t) \equiv \mathbf{R}_\alpha(t) - \mathbf{R}_\beta(t)$. The stress tensor has thus become a nonlinear function of $\nabla\boldsymbol{\eta}(\mathbf{r},t)$. Note that its time dependence arises both from the time dependence of $\boldsymbol{\eta}(\mathbf{r},t)$ and from the leading-order motion of the lattice in the laminar flow.

Expanding Eqs. (2.7) and (2.8) in powers ξ^{-1} and expressing the result in cylindrical coordinates gives

$$\begin{aligned} D_t^2\eta_r - 2\Omega(D_t\eta_\phi - r\Omega'\eta_r) &- \nu\left[\left[\nabla^2 - \frac{1}{r^2}\right]D_t\eta_r - \frac{2}{r^2}\frac{\partial(D_t\eta_\phi - r\Omega'\eta_r)}{\partial\phi}\right] \\ &= \frac{\rho_c f_r(\mathbf{r},t)}{\rho m_c} - \frac{\partial\delta p_h}{\partial r}, \end{aligned} \tag{2.10}$$

$$\begin{aligned} D_t^2\eta_\phi + 2\Omega D_t\eta_r &- \nu\left[\left[\nabla^2 - \frac{1}{r^2}\right](D_t\eta_\phi - r\Omega'\eta_r) + \frac{2}{r^2}\frac{\partial(D_t\eta_r)}{\partial\phi}\right] \\ &= \frac{\rho_c f_\phi(\mathbf{r},t)}{\rho m_c} - \frac{1}{r}\frac{\partial\delta p_h}{\partial\phi}, \end{aligned} \tag{2.11}$$

and

$$D_t^2\eta_z - \nu\nabla^2 D_t\eta_z = \frac{\rho_c f_z(\mathbf{r},t)}{\rho m_c} - \frac{\partial\delta p_h}{\partial z}, \tag{2.12}$$

where $\rho_c(\mathbf{r},t)$ is the mass density of colloidal which is treated as a constant over scales much larger than the lattice spacing, $\rho \equiv \rho_f + \rho_c$, and ν is the kinematic viscosity.

The incompressibility condition for the underlying fluid, i.e., $\nabla\cdot\mathbf{v}(\mathbf{r},t) = 0$, requires that $D_t\nabla\cdot\boldsymbol{\eta} = 0$, thereby implying that $\nabla\cdot\boldsymbol{\eta}$ is a constant along a streamline. However, $\boldsymbol{\eta}$ must either be quasiperiodic in time or decay to zero in the long time limit for nonchaotic motion. In either case, $\nabla\cdot\boldsymbol{\eta}$ cannot be any constant other than zero, and therefore the incompressibility condition becomes

$$\nabla\cdot\boldsymbol{\eta} = 0. \tag{2.13}$$

For the purposes of a linear stability analysis, the stress may be further expanded to linear order in $\nabla\boldsymbol{\eta}$. As discussed in Ref. [4] and Appendix A, this suggests the following model expression:

$$\mathbf{f}(\mathbf{r},t) = \frac{\rho m_c c^2}{\rho_c}[1 + 2\epsilon\cos(\Gamma t)]\nabla^2\boldsymbol{\eta}(\mathbf{r},t), \tag{2.14}$$

where

$$\Gamma \equiv \frac{R_1\Omega_1 - R_2\Omega_2}{R_1 - R_2} \tag{2.15}$$

is average velocity gradient in r direction and $\epsilon < 0.5$. The term in ϵ models the modulation of the local elastic constants that results from the periodic distortion of the crystal lattice caused by the laminar flow. We have ignored the contributions of higher-order harmonics and have replaced the local modulation rate (i.e., the local velocity gradient) by the average gradient Γ. This last assumption should be valid as long as the distance between the inner and outer cylinders is small compared with the radii. Finally, as was done in Ref. [4], we have assumed that the system is locally isotropic, at least for the purposes of calculating the elastic moduli. Should this not be the case, the acoustic mode structure will be slightly more complicated; nonetheless the basic physical ideas presented here will still be valid.

By defining $\bar{\eta}_{\{r,\phi,z\}} \equiv \sqrt{r}\, e^{-i(m\phi + k_z z)}\eta_{\{r,\phi,z\}}(\mathbf{r},t)$ and eliminating δp_h in Eqs. (2.10)–(2.12), we find that

$$
\begin{aligned}
0={}&D_t^2\bar{\eta}_r-2\Omega(D_t\bar{\eta}_\phi-r\Omega'\bar{\eta}_r)\\
&-c(t)^2\left[\left(\Delta-\frac{1}{r^2}\right)\bar{\eta}_r-\frac{2im}{r^2}\bar{\eta}_\phi\right]\\
&-\nu\left[\left(\Delta-\frac{1}{r^2}\right)D_t\bar{\eta}_r-\frac{2im}{r^2}(D_t\bar{\eta}_\phi-r\Omega'\bar{\eta}_r)\right]\\
&-\frac{1}{k_z^2}D_r^-[D_t^2-\nu\Delta D_t-c(t)^2\Delta]\left(D_r^+\bar{\eta}_r+\frac{im}{r}\bar{\eta}_\phi\right),
\end{aligned}
\tag{2.16}
$$

$$
\begin{aligned}
0={}&D_t^2\bar{\eta}_\phi+2\Omega D_t\bar{\eta}_r\\
&-c(t)^2\left[\left(\Delta-\frac{1}{r^2}\right)\bar{\eta}_\phi+\frac{2im}{r^2}\bar{\eta}_r\right]\\
&-\nu\left[\left(\Delta-\frac{1}{r^2}\right)(D_t\bar{\eta}_\phi-r\Omega'\bar{\eta}_r)+\frac{2im}{r^2}D_t\bar{\eta}_r\right]\\
&-\frac{im}{k_z^2 r}[D_t^2-\nu\Delta D_t-c(t)^2\Delta]\left(D_r^+\bar{\eta}_r+\frac{im}{r}\bar{\eta}_\phi\right),
\end{aligned}
\tag{2.17}
$$

and

$$D_r^+\bar{\eta}_r+\frac{im}{r}\bar{\eta}_\phi+ik_z\bar{\eta}_z=0, \tag{2.18}$$

where

$$c(t)\equiv c[1+2\epsilon\cos(\Gamma t)]^{1/2},$$

$$D_t\equiv\frac{\partial}{\partial t}+im\Omega(r),$$

$$\Delta\equiv\frac{\partial^2}{\partial r^2}-\frac{m^2-1/4}{r^2}-k_z^2,$$

and

$$D_r^\pm\equiv\frac{\partial}{\partial r}\pm\frac{1}{2r}.$$

Furthermore, if $k_z=0$, we find that $\bar{\eta}_z$ completely decouples from other components of $\boldsymbol{\eta}$, i.e.,

$$[D_t^2-\nu\Delta D_t-\Delta c(t)^2]\bar{\eta}_z=0. \tag{2.19}$$

III. LINEAR STABILITY ANALYSIS

We now analyze the stability of the laminar state under shear. The analysis is standard and is laid out in detail in Ref. [4]. In short, we expand the space dependence of $\bar{\eta}_r(r,t)$ and $\bar{\eta}_\phi(r,t)$ in an complete orthonormal set of functions $\{\psi_n(r)\}$, which are defined for $r\in[R_1,R_2]$. The no-slip boundary conditions imply that both $\psi_n(r)$ and $\psi_n{}'(r)$ vanish at $R=R_1,R_2$ [10]. It is then easy to rewrite Eqs. (2.16) and (2.17) in first-order matrix form $\dot{y}=My$, where M is the matrix representation of the operator

$$\hat{M}=\begin{bmatrix}0 & -1\\ -\hat{A}^{-1}\hat{C}(t) & -\hat{A}^{-1}\hat{B}\end{bmatrix}. \tag{3.1}$$

The operators $\hat{A}$, $\hat{B}$, and $\hat{C}(t)$ corresponding to Eqs. (2.16) and (2.17) are listed in Appendix B.

In the actual computations, we take [6]

$$
\psi_{n,\text{parity}}(r)\equiv\begin{cases}
N_{\text{even}}^{-1}\left[\dfrac{\cos(S_n x)}{\cos(S_n L)}-\dfrac{\cosh(S_n' x)}{\cosh(S_n' L)}\right] & \text{(even parity)}\\[2ex]
N_{\text{odd}}^{-1}\left[\dfrac{\sin(K_n x)}{\sin(K_n L)}-\dfrac{\sinh(K_n' x)}{\sinh(K_n' L)}\right] & \text{(odd parity),}
\end{cases}
\tag{3.2}
$$

where $L\equiv(R_2-R_1)/2$, $r\equiv x+(R_1+R_2)/2$, and $N_{\text{even (odd)}}$ are normalization constants defined by requiring that

$$\int_{R_1}^{R_2}dr\,|\psi_{n,\alpha}(r)|^2=1.$$

S_n, S_n', K_n, and K_n' satisfy

$$S_n\tan(S_nL)+S_n'\tanh(S_n'L)=0 \tag{3.3}$$

and

$$K_n\tanh(K_n'L)-K_n'\tan(K_nL)=0, \tag{3.4}$$

where $S_n'^2-S_n^2=K_n'^2-K_n^2=\kappa^2$, where we usually set κ to zero.

A similar procedure can be applied to Eq. (2.19) when $k_z=0$. The resulting analysis is much simpler; $\hat{A}$ becomes the identity

$$\hat{B}=-\nu\Delta+2im\Omega(r), \tag{3.5}$$

and

$$\hat{C}(t)=-m^2\Omega^2(r)-im\nu\Delta\Omega(r)-c^2[1+2\epsilon\cos(\Gamma t)]\Delta. \tag{3.6}$$

In this case it is simpler to use sinusoidal functions as the basis. Equations (2.16) and (2.17) are more general for $k_z\neq 0$, and better convergence is expected when the basis defined by Eq. (3.2) is used since these functions satisfy all the boundary conditions for the problem. On the other hand, $k_z=0$ will turn out to be the physically relevant case; hence Eq. (2.19) will apply and the simpler sinusoidal basis may be used.

No matter which basis is chosen, the resulting system of ordinary differential equations is a set of coupled Mathieu-Hill equations [4,11,12] and may be studied using Floquet's theorem; i.e., we write the solutions to the expanded equations in the form $y(t)=e^{\mu t}y_p(t)$, where $y_p(t)$ is periodic with period $2\pi/\Gamma$, and μ is the Floquet exponent. The system is locally stable as long as $\text{Re}(\mu)<0$. Hence, for a given set of parameters, we look for the lowest angular velocity for which $\text{Re}(\mu)$ vanishes.

The periodic function $y_p(t)$ is expanded as a discrete Fourier series in time and the Floquet exponents are computed by finding the zeros of the Hill's determinant or, equivalently, by examining the eigenvalues of the matrix which results after Fourier analyzing M in time. The point at which the expansions are truncated is varied until there is no significant change in the results; for the material parameters considered below, convergence is obtained when 10 spatial and 11 temporal (when $\epsilon \neq 0$) basis functions are used.

When the elastic forces are switched off, i.e., when $c=0$, it is easy to show that Eqs. (2.16) and (2.17) are equivalent to the usual Navier-Stokes equations for Taylor-Couette flow [6], and hence Taylor-roll instabilities result. On the other hand, if $c \neq 0$, i.e., when intercolloid interactions are included, forming a Taylor roll requires that the colloid lattice be deformed into a roll. This requires energy, and it is not surprising that the system becomes more stable to these kinds of deformations.

This suppression of the Taylor instability is examined in Fig. 1(a). When $c=0$, the Taylor instability occurs at the expected inner cylinder rotation rate and the roll has the expected periodicity in the z direction. The Taylor instability is shifted to higher rotation rates as the crystal is made more rigid. For typical colloidal crystals, the speed of sound is roughly 10 cm/sec and convection related (such as Taylor) instabilities are strongly suppressed at low shear rates; cf. Fig. 1(b).

We can find stability boundaries which correspond to instabilities that are qualitatively similar to those found in the usual Taylor instability. Floquet exponents for these modes are shown in Fig. 1(c). While the mode [in the specified (k_z, m) plane] to first go unstable is slightly different than the usual Taylor instability, cf. the inset, the continuation of the mode corresponding to the usual Taylor instability will end up growing faster at high rotation rates, and should result a more usual Taylor-roll pattern being formed. This is observed in the experiments of Weitz, Dozier, and Chaikin. The change to a more usual pattern encountered in Taylor flow should be expected because the convective terms which drive the Taylor instability at some point will dominate the elastic ones (remember that colloidal crystals are extremely soft).

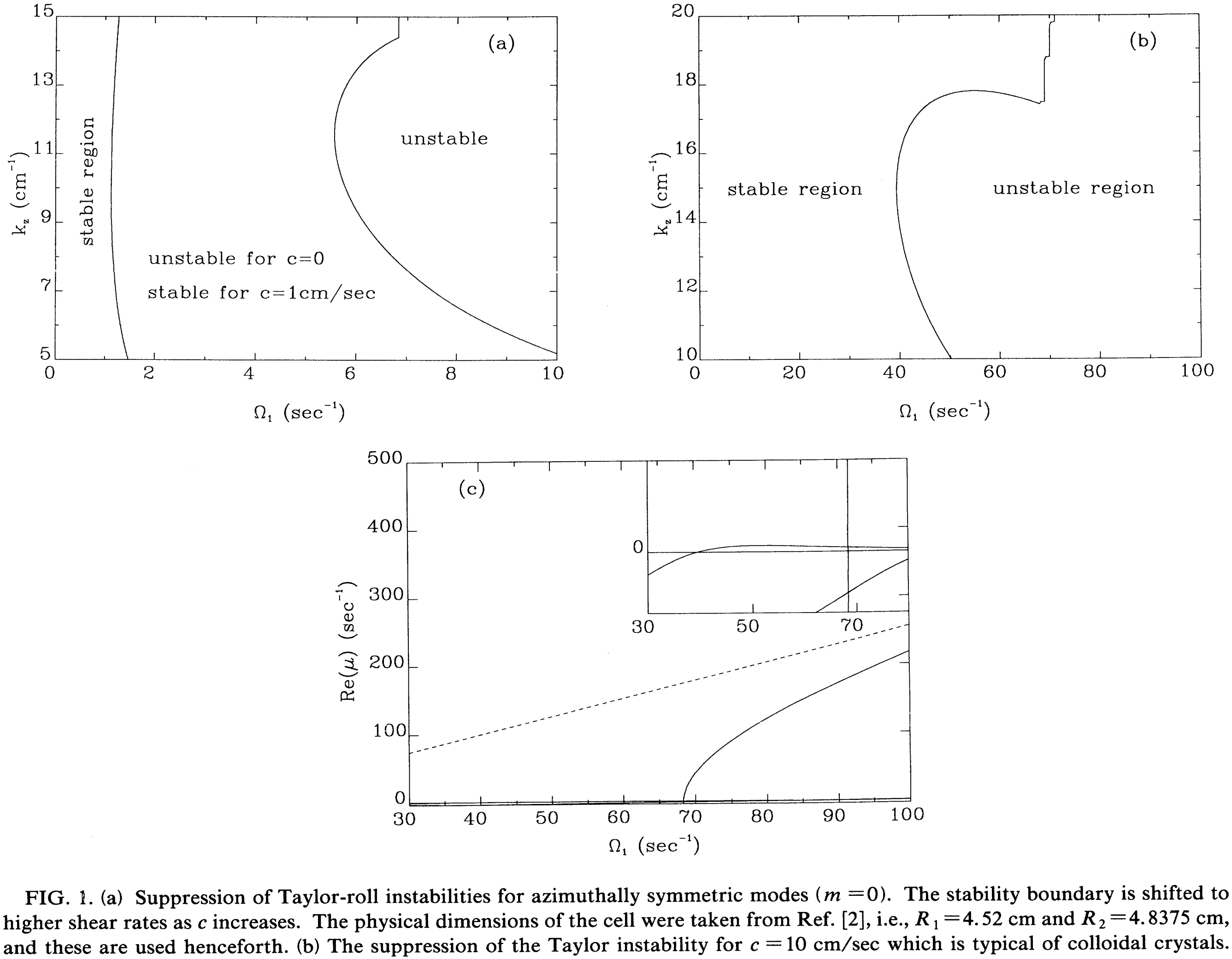

FIG. 1. (a) Suppression of Taylor-roll instabilities for azimuthally symmetric modes ($m=0$). The stability boundary is shifted to higher shear rates as c increases. The physical dimensions of the cell were taken from Ref. [2], i.e., $R_1=4.52$ cm and $R_2=4.8375$ cm, and these are used henceforth. (b) The suppression of the Taylor instability for $c=10$ cm/sec which is typical of colloidal crystals. The remaining parameters are the same as in Fig. 1(a). (c) Plot of the largest growth exponents Re(μ) as a function of Ω_1 for $c=10$ cm/sec, $k_z=15$ cm^{-1}, and $m=0$. The dashed line is the result for the usual Taylor problem, i.e., $c=0$. The inset shows the details near the onset of the instability in the specified (k_z, m) plane. Note that the mode associated with the line which approaches the fastest growing mode found in the Taylor instability is not the first mode to become unstable.

For reasonable values of the material parameters, the Taylor-like instabilities discussed in the preceding paragraph are not the first to occur. They are preempted by one of two resonance instabilities. By this we refer to an instability which occurs only when the rotation rates are tuned to some narrow range of values. The motion is stable either above or below this range, and the system has only narrow bands of unstable modes. Two types of these instabilities have been found numerically: one which strongly depends on ϵ and the other is practically independent of ϵ. In addition, Figs. 1(a) and 1(b) assume axisymmetric flow ($m=0$), and as we shall now show, axisymmetric modes are not the first ones to become unstable.

A. Mathieu instabilities

The first class of instabilities is qualitatively similar to those discussed for the plane Couette flow in Ref. [4]; namely Mathieu instabilities that occur when the modulation frequency of the crystal elastic properties (i.e., Γ) is an integer subharmonic of twice a natural oscillation frequency of the system. The behavior is somewhat more complicated than that found in the usual analysis of the Mathieu instability due to the presence of viscosity, the large number of modes, and convective effects which change the $\epsilon=0$ frequencies and lifetimes of the colloidal crystal transverse acoustic modes (cf. Ref. [4]).

Some results for the Floquet exponents are shown in Figs. 2(a)–2(c). The data show several phenomena. First, we see that modes roughly come in pairs. Each of the pairs of modes corresponds to underdamped transverse acoustic modes that propagate relative to the mean rotation in clockwise and counterclockwise directions. While time-reversal invariance normally requires that each of the pairs have the same decay rate, here the rotation breaks this symmetry, with the mode propagating ahead of the laminar rotation having a slightly longer lifetime.

An onset of instability is seen in Fig. 2(a) near $\Omega_1 \approx 10.6 \text{ sec}^{-1}$ (or 1.69 Hz and corresponding to a shear rate of roughly 25 Hz). This is a Mathieu instability and involves both clockwise and counterclockwise propagating (relative to the laminar rotation) transverse acoustic modes. The ϵ dependence of the imaginary part of the Floquet exponent is shown in Fig. 2(b). As in Ref. [4], reducing the modulation amplitude (ϵ) stabilizes the mode, as shown in Fig. 2(c).

Of course, finding a single instability is not sufficient. We need to know the lowest rotation rate that makes *any* mode unstable. The m dependence of the first unstable region is shown in Fig. 3. (It is easy to see that the critical line is even under $m \rightarrow -m$ and $k_z \rightarrow -k_z$.) A "finger" of instability is shown that is qualitatively similar to those found in Ref. [4]. As m is increased, viscous effects become more important and the motion becomes stable.

The data shown in Figs. 2 and 3 were computed for $k_z=0$. Our numerical work shows that increasing k_z raises the critical rotation rate of the first unstable mode. This can again be understood in terms of viscous effects.

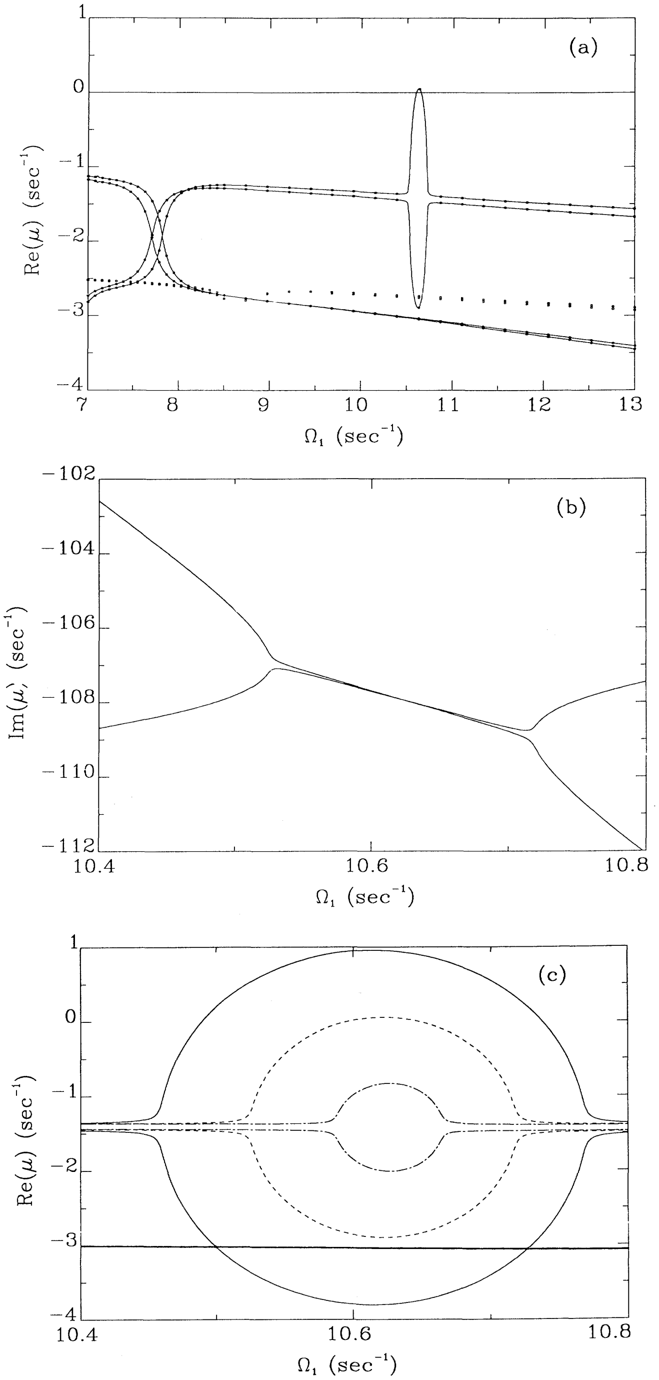

FIG. 2. (a) Floquet exponents at the first Mathieu instability. This figure shows the real part of the exponent near the onset of Mathieu instability when $c=10$ cm/sec, $\epsilon=0.05$, $m=36$, and $k_z=0$. The points indicate modes as computed from Eqs. (2.16) and (2.17), while the solid lines are those computed from Eq. (2.19). The extra pair of modes correspond to a transverse displacement in the r-ϕ plane, which is only contained in Eqs. (2.16) and (2.17). (b) The imaginary parts of the Floquet exponents for the two modes involved in the first Mathieu instability shown in (a). (c) The ϵ dependence of $\text{Re}(\mu)$ for the cases shown in (a) and (b). If ϵ is too small, the motion will not become unstable. The curves correspond to values of ϵ as follows: 0.08 (solid), 0.05 (dashed), and 0.02 (dot dashed).

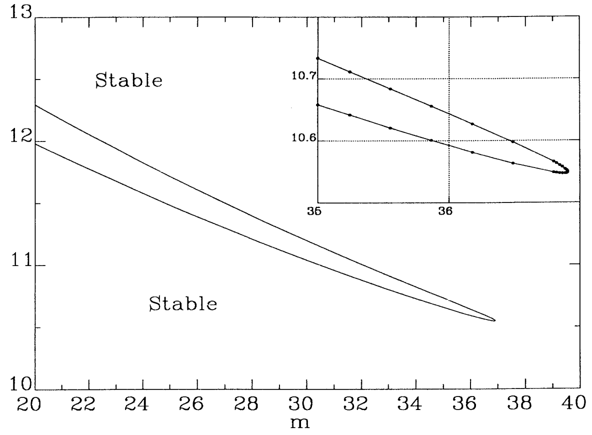

FIG. 3. Stability boundary of the first Mathieu unstable region for $c = 10$ cm/sec, $\epsilon = 0.05$, and $k_z = 0$.

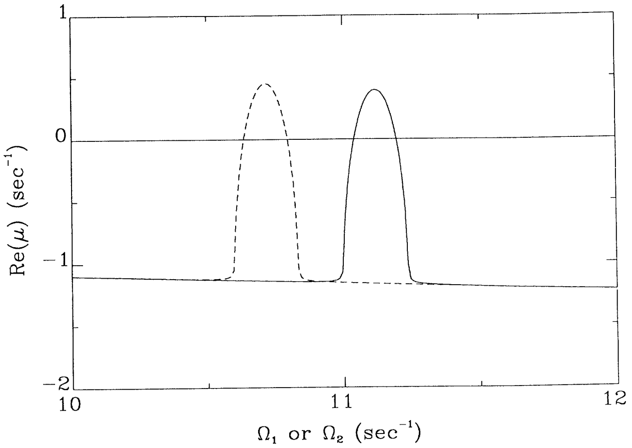

FIG. 4. The changes in the Floquet exponents when the inner or outer cylinder is rotated. The solid (dashed) curve shows the case when outer (inner) cylinder is at rest while Ω_1 (Ω_2) is nonzero for $c = 10$ cm/sec, $m = 30$, $\epsilon = 0.05$, and $k_z = 0$. Note that unlike the Taylor instability, the Mathieu instability should occur even if the outer cylinder is rotated.

From the data shown in Fig. 3, we see that the marginal state has $m = 36$ (remember that physical values of m must integer) and $\Omega_1 = 10.6$ sec^{-1}. In addition, Im$(\mu) = -108.0$ sec$^{-1} \neq 0$ at the instability, and hence exchange of stability does not occur [13].

The first unstable mode has $\boldsymbol{\eta}(\mathbf{r},t)$ pointing entirely in the z direction. This may be understood in terms of the transverse normal mode frequencies in the absence of shear. For $k_z = 0$ we have seen, cf. Eq. (2.19), that the $\eta_z(\mathbf{r},t)$ decouples from the ϕ and r components. When $m \neq 0$ the r and ϕ displacements must be coupled in order that the incompressibility condition be satisfied, and hence the coupled motion requires more elastic energy than motion in the z direction. This results in a higher vibrational frequency, and the resonance condition required for the occurrence of a Mathieu instability occurs later. Therefore, we conclude that

$$\boldsymbol{\eta}\cdot\nabla\mathbf{v} = 0, \quad \boldsymbol{\eta}\cdot\nabla\boldsymbol{\eta} = 0 \tag{3.7}$$

at the instability. Note that our conclusion is dependent on the isotropic form assumed for the elastic moduli. If this is not the case, then it is possible that the r-ϕ motions would become unstable first if they remain uncoupled from the z motion and if the transverse sound speed for these motions was much lower than that for the z motion. In addition, note that the elastic constants for the sheared crystal are likely to be somewhat different than those in the equilibrium state.

Finally we compare the cases of rotating the outer vs inner cylinders in Fig. 4. Unlike the Taylor instability, the Mathieu instability only requires that the elastic property modulation rate be resonant, and this in turn only depends on the magnitude of the local shear gradient. Figure 4 supports this conclusion, although it is important to remember that

$$\frac{\Omega_1\ (\text{as } \Omega_2 = 0)}{\Omega_2\ (\text{as } \Omega_1 = 0)} = \frac{R_2}{R_1} \tag{3.8}$$

when $|\Gamma|$ remains unchanged. In addition, there are small effects associated with the Coriolis and centrifugal terms in the equations of motion that differentiate between inner and outer cylinder rotation. (For the data shown in Fig. 4, $\Omega_2/\Omega_1 = 0.963$ at the corresponding instability points, while $R_1/R_2 = 0.934$.) In the limit of plane Couette flow, the two peaks in Fig. 4 merge.

Finally, we show an example of real and imaginary parts of the displacement field at the marginal state in Fig. 5. The marginal state is quasiperiodic, although the complex magnitude of the displacement field is periodic with period $2\pi/\Gamma$.

It is interesting to note that in Ref. [2], Weitz, Dozier, and Chaikin reported the observation of vertical stripe

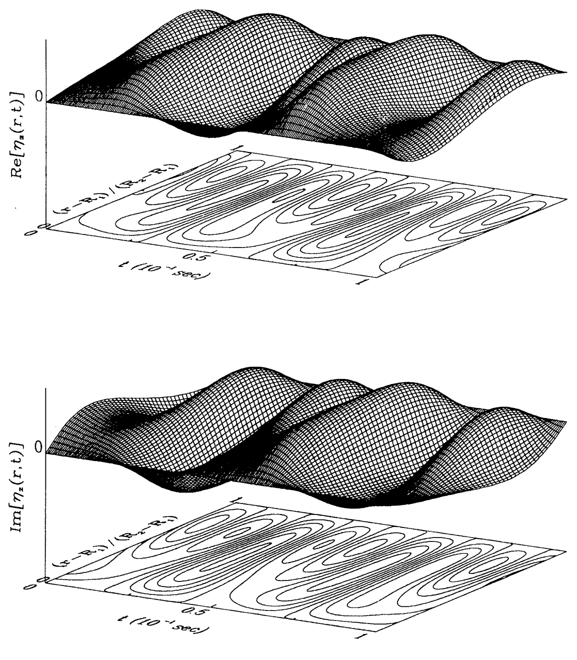

FIG. 5. Real and imaginary parts of $\eta_z(\mathbf{r},t)$ at the onset of first Mathieu instability shown in Figs. 2 and 3.

TABLE I. Critical mode parameters for $c = 7$ cm/sec.

ϵ	Ω_1 (sec^{-1})	m	$2\pi R_2/m$ (cm)
0.04	8.3	23	1.32
0.05	8.13	28	1.09
0.06	7.86	32	0.95

patterns in alternating colors when the shear rate is about 10 Hz. The wavelength of the pattern is about 1 cm. For $\epsilon = 0.05$ and $c = 10$ cm/sec, our numerical work shows that the mode with $m = 36$ and $k_z = 0$ is the first to become unstable (this is a Mathieu instability) at $\Omega_1 = 10.6\ \text{sec}^{-1}$ (1.69 Hz). This corresponds to a vertical stripe pattern with a wavelength of about 0.84 cm.

The critical rotation rate and number of stripes depends on the sound speed and on ϵ. Some results for a system having one of the sound speeds reported in Ref. [2] are summarized in Table I.

B. Acoustic instabilities

In addition to the Mathieu instabilities just discussed, there is another class of resonance like instabilities that is essentially independent of the value of ϵ. The decay rates for the first few linearized modes in the relevant range of parameters are shown in Fig. 6. An instability is clearly shown, and this one has practically no dependence on ϵ, at least for physical values of ϵ (i.e., $\epsilon < 0.5$). As was the case in the Mathieu instabilities, the first mode to become unstable corresponds to vertically uniform motion [i.e., $k_z = 0$, $m \neq 0$, and $\eta(\mathbf{r}, t) \| \hat{\mathbf{z}}$], and hence Eq. (3.7) is valid here as well.

This instability bears no relation to the Mathieu instabilities since it is independent of ϵ. Nonetheless, it occurs as a resonance and only appears if the rotation rate is adjusted to some small range of values (strictly speaking, for fixed m and k_z). It is natural to ask what is the mechanism for this instability.

In trying to understand this resonance, it is convenient to introduce reduced units by letting $L \equiv (R_2 - R_1)/2$, $\tau L \equiv ct$, $xL \equiv r - (R_2 + R_1)/2$, $\hat{q} \equiv mL/R_1$, $\hat{\omega} \equiv \Omega_1 R_1 / 2c$, $\hat{\nu} \equiv \nu / Lc$, and $f \equiv \bar{\eta}_z e^{-im\Omega_1 t/2}$. Then, in the narrow-gap limit, i.e., where we take $\Omega(r)$ as a linear function of x, Eq. (2.19) becomes

$$\left\{ \frac{\partial^2}{\partial \tau^2} + \left[\hat{\nu} \left[\hat{q}^2 - \frac{\partial^2}{\partial x^2} \right] - 2i\hat{\omega}\hat{q}x \right] \frac{\partial}{\partial \tau} + \left[\hat{q}^2 - \frac{\partial^2}{\partial x^2} \right] - \hat{\omega}^2 \hat{q}^2 x^2 - i\hat{\nu}\hat{\omega}\hat{q} \left[\hat{q}^2 x - x\frac{\partial^2}{\partial x^2} - 2\frac{\partial}{\partial x} \right] \right\} f(x,\tau) = 0. \tag{3.9}$$

In order to see how the instability arises, we ignore the viscosity, and set $\hat{\nu} = 0$. Noting that $f(\pm 1, \tau) = 0$, and assuming that solutions are marginal, i.e., f is independent of time, we find that

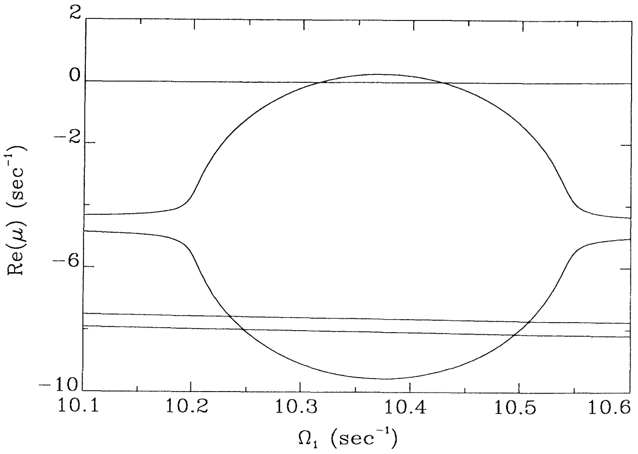

FIG. 6. An example of the acoustic instability when $c = 10$ cm/sec, $\epsilon = 0$, $k_z = 0$, and $m = 88$.

$$\left[-\frac{1}{2} \frac{\partial^2}{\partial x^2} + V(x) \right] f = Ef, \tag{3.10}$$

where $E = 0$ and

$$V(x) = \begin{cases} \frac{1}{2}\hat{q}^2(1 - \hat{\omega}^2 x^2), & |x| < 1 \\ +\infty, & |x| \geq 1. \end{cases} \tag{3.11}$$

Equation (3.10) has been cast in the form of the time independent Schrödinger equation for a one-dimensional problem with potential $V(x)$. Of course, the additional condition $E = 0$ requires that we adjust $\hat{\omega}$ so that there is an eigenvalue $E = 0$, and the onset of instability will occur the first time such an eigenstate occurs. With the problem cast in this manner, it is obvious that a necessary condition for the existence of an $E = 0$ solution is that minimum value of the potential be negative, and hence

$$\hat{\omega} > 1. \tag{3.12}$$

When this condition is expressed in terms of the original variables, we see that the rotation must be supersonic, i.e., the velocity difference between the walls and center of the cell exceeds the transverse speed of sound in the crystal.

The potential $V(x)$ given by Eq. (3.11) only has discrete eigenstates, and hence the values of $\hat{\omega}$ at which marginal solutions occur will also be discrete. As $\hat{\omega}$ is increased, the number of states with $E < \frac{1}{2}\hat{q}^2$ will increase and move to lower energy, ultimately passing through zero. Each time this happens, there will be a resonantlike instability.

The quantum-mechanical analogy sheds light on the forms of the displacement fields. Specifically, they will be oscillatory for $\hat{\omega}^{-1} < |x| < 1$ and will decay exponentially into the middle of the cell. Hence, as the shear rate is increased, the marginal acoustic fluctuations will be confined to narrow boundary layers near the walls. In addition, for larger shear rates the resonances will come in closely spaced pairs, the splitting being simply related to the usual tunneling splitting for the barrier.

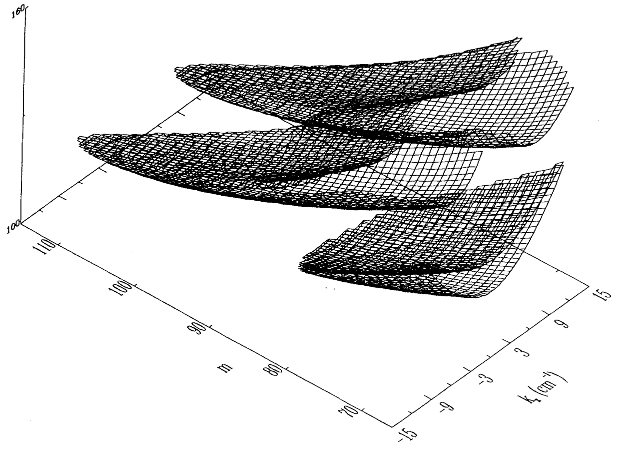

FIG. 7. Unstable (acoustic) regions as function of k_z and m with $c = 10$ cm/sec.

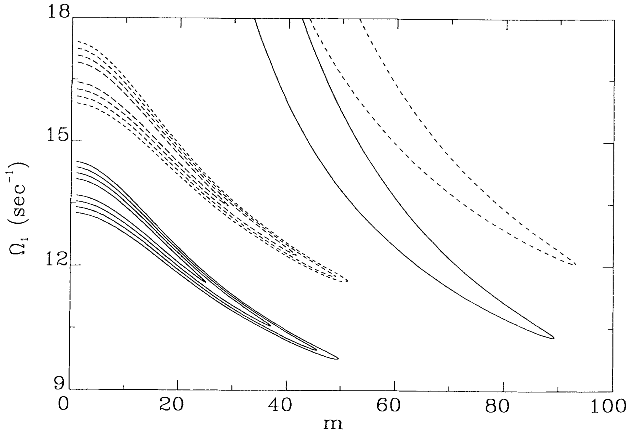

FIG. 9. Mathieu and acoustic unstable regions for several values of ϵ; specifically, 0.09, 0.07, 0.05, and 0.03. Note that the acoustic unstable regions (at the upper right) are unchanged when ϵ is changed, while the Mathieu unstable regions (lower left) shrink when ϵ decreases. The acoustic instability can occur before (for ϵ = 0.05 and 0.03) or after (for $\epsilon = 0.09$ and 0.07) the Mathieu instability. Moreover, reducing the speed of sound also makes the first instability occur earlier, and the behavior for $c = 10$ cm/sec (solid) and $c = 12$ cm/sec (dashed) is shown.

This analysis is certainly not complete since viscosity is ignored and k_z was set to zero. Nonetheless, it shows that Eq. (3.9), and hence Eq. (2.19), has resonant instabilities independent of the value of ϵ. Further analysis shows that the mode with $k_z = m = 0$, cf. Eq. (3.9), is stable with respect to this type resonance.

We have numerically analyzed the full equations in the supersonic region. As was the case with the Mathieu instabilities, increasing k_z leads to an increase in the critical rotation rate needed for instability and introduces other resonances with $\eta_{r,\phi} \neq 0$. An example of how the unstable regions change as a function of k_z and m is shown in Fig. 7, and an example of the displacement field at the first acoustic instability point is shown in Fig. 8. Note that unlike the Mathieu instabilities, here the amplitude of the unstable mode is approximately constant in time and the phase is nonuniform in space; it can be written as $\mathrm{Im}(\mu)t + \delta(r)$. This is expected since the equations are separable in time when $\epsilon = 0$.

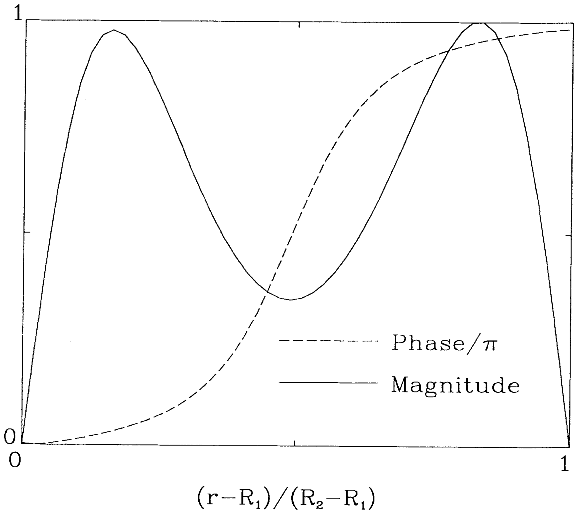

FIG. 8. A plot of $|\eta_z(r,0)|$ (solid) and the phase shift $\delta(r)$ (dashed) at the onset of an acoustic instability: $m = 89$, $k_z = 0$, $\Omega_1 = 10.3$ sec^{-1}, and $c = 10$ cm/sec.

Finally, the instability regions corresponding to the first instability for the two resonance mechanisms in the $k_z = 0$ plane are compared in Fig. 9. As the figure shows, the acoustic instabilities are at higher values of m and they can come either before or after the Mathieu instabilities depending on values of c and ϵ. Note that the values of m at the first acoustic instability (i.e., the number of stripes) is 88 for $c = 10$ cm/sec and $\epsilon = 0$, and occurs at $\Omega_1 = 10.3$ sec^{-1}.

Weitz, Dozier, and Chaikin [2] report sometimes observing metastable patterns with much smaller spacing between the stripes (~ 3 mm). For their experimental geometry this corresponds to $m \sim 98$, although if this pattern is related to the acoustic instability discussed here, the sound speed of the crystal must be known accurately before a detailed comparison can be made.

IV. NONLINEARITIES AND AMPLITUDE EQUATIONS

The preceding section focused on linear stability analysis. Of course, once the system becomes unstable, the displacement field begins to grow exponentially in time and the linearized equations will no longer be valid; nonlinear terms must be included in order to proceed further. As discussed in the preceding section, we are most interested in the Mathieu instability, since the marginal state bears some resemblance to what is observed experimentally and since it will be the first to occur for all but extremely small values of the modulation amplitude ϵ. This must be born in mind when considering various nonlinear corrections.

Nonlinear terms arise from several sources: (1) the nonlinear convective terms in the equations of motion; (2) the nonlinear correction terms in the relationship between the colloid particle positions and the displacement field, cf. Eq. (2.5); and (3) anharmonic elastic interactions. The role of the convective terms is expected to be small for low rotation rates. Moreover, if the convective terms can be treated perturbatively, then Eq. (3.7) guarantees that the convection terms vanish at *all* orders, and hence the symmetry of the marginal state will be manifested in the unstable ones. In addition, it is easy to see that the nonlinear corrections to Eq. (2.5) will also vanish for vertically striped states where the displacement is the direction of the stripes. Thus the only remaining source of nonlinearity is the anharmonic contribution to the elastic interactions, and these are discussed in Appendix A.

By including the nonlinear terms, cf. Eqs. (A7) and (A8), in Eq. (2.12), and remembering that $k_z=0$, we find that

$$\left[\frac{\partial}{\partial t}+\mathbf{v}\cdot\nabla\right]^2\eta_z-\nu\nabla^2\left[\frac{\partial}{\partial t}+\mathbf{v}\cdot\nabla\right]\eta_z$$
$$=c(t)^2\nabla^2\eta_z+\nabla\cdot[(b|\nabla\eta_z(\mathbf{r},t)|^2+d|\nabla\eta_z(\mathbf{r},t)|^4+\dots)\nabla\eta_z(\mathbf{r},t)], \tag{4.1}$$

where b and d are determined by the details of the lattice and intercolloidal interactions. As was the case with the coefficients of the linear elasticity terms, the anharmonic coupling parameters will be a periodic functions of time for sheared lattices. Here, however, we ignore this time dependence for simplicity.

We will solve the nonlinear equation of motion by expanding $\eta_z(\mathbf{r},t)$ in some complete set of space-dependent functions with time dependent amplitudes. Specifically, for z-independent solutions, we let

$$\eta_z(r,\phi,t)\equiv\sum_m\sum_j\frac{1}{\sqrt{r}}\psi_j(r)e^{im\phi}A_j^{(m)}(t), \tag{4.2}$$

where the ψ's are a normalized sine basis. Equations of motion for the amplitudes are found by projecting Eq. (4.1) onto $\psi_j(r)e^{im\phi}/(2\pi r^{1/2})$. We thereby find that

$$0=\ddot{A}_j^{(m)}(t)+\sum_k[B_{jk}\dot{A}_k^{(m)}(t)+C(t)_{jk}A_k^{(m)}(t)]+b\sum_{\substack{j_1,j_2,j_3\\m_1+m_2+m_3=m}}I_{j;j_1,j_2,j_3}^{m;m_1,m_2,m_3}A_{j_1}^{(m_1)}(t)A_{j_2}^{(m_2)}(t)A_{j_3}^{(m_3)}(t)$$
$$+d\sum_{\substack{j_1,j_2,j_3,j_4,j_5\\m_1+m_2+m_3+m_4+m_5=m}}J_{j;j_1,j_2,j_3,j_4,j_5}^{m;m_1,m_2,m_3,m_4,m_5}A_{j_1}^{(m_1)}(t)A_{j_2}^{(m_2)}(t)A_{j_3}^{(m_3)}(t)A_{j_4}^{(m_4)}(t)A_{j_5}^{(m_5)}(t)+\cdots, \tag{4.3}$$

where

$$I_{j;j_1,j_2,j_3}^{m;m_1,m_2,m_3}\equiv\int_{R_1}^{R_2}\frac{dr}{r^5}[\hat{\psi}_j(r)\hat{\psi}_{j_1}(r)+mm_1\psi_j(r)\psi_{j_1}(r)][\hat{\psi}_{j_2}(r)\hat{\psi}_{j_3}(r)-m_2m_3\psi_{j_2}(r)\psi_{j_3}(r)], \tag{4.4a}$$

$$J_{j;j_1,j_2,j_3,j_4,j_5}^{m;m_1,m_2,m_3,m_4,m_5}\equiv\int_{R_1}^{R_2}\frac{dr}{r^8}[\hat{\psi}_j(r)\hat{\psi}_{j_1}(r)+mm_1\psi_j(r)\psi_{j_1}(r)]$$
$$\times[\hat{\psi}_{j_2}(r)\hat{\psi}_{j_3}(r)-m_2m_3\psi_{j_2}(r)\psi_{j_3}(r)][\hat{\psi}_{j_4}(r)\hat{\psi}_{j_5}(r)-m_4m_5\psi_{j_4}(r)\psi_{j_5}(r)], \tag{4.4b}$$

$$\hat{\psi}_j(r)\equiv\left[r\frac{d\psi_j(r)}{dr}-\frac{1}{2}\psi_j(r)\right],$$

and B_{jk} and $C_{jk}(t)$ are matrix elements of $\hat{B}$ and $\hat{C}(t)$ defined by Eqs. (3.5) and (3.6).

Since $\eta_z(r,\phi,t)$ is real, Eq. (4.2) implies that $A_j^{(-m)}(t)=A_j^{(m)*}(t)$. From Fig. 3 we see that when the first m state becomes unstable the others are still stable, and in addition, the unstable regions are very narrow for small ϵ; hence, even within the unstable region, only a single value of m is usually found to be unstable, although the m value of the unstable mode will decrease with increasing shear rate. We therefore assume that the dominant contribution to the sums in Eq. (4.3) comes from the terms with $|m_1|=|m_2|=\cdots=|m|$ and ignore the rest; we thus find that

$$0=\ddot{A}_j^{(m)}(t)+\sum_{k=1}^{N}[B_{jk}\dot{A}_k^{(m)}(t)+C(t)_{jk}A_k^{(m)}]+b\sum_{j_1,j_2,j_3}K_{j;j_1,j_2,j_3}^{(m)}A_{j_1}^{(m)}(t)A_{j_2}^{(m)^*}(t)A_{j_3}^{(m)}(t)$$
$$+d\sum_{j_1,j_2,j_3,j_4,j_5}L_{j;j_1,j_2,j_3,j_4,j_5}^{(m)}A_{j_1}^{(m)}(t)A_{j_2}^{(m)^*}(t)A_{j_3}^{(m)^*}(t)A_{j_4}^{(m)}(t)A_{j_5}^{(m)}(t)+\cdots, \tag{4.5}$$

where $j=1,\ldots,N$, N is the point at which the basis expansion is truncated,

$$K^{(m)}_{j;j_1,j_2,j_3} \equiv 2I^{m;m,-m,m}_{j;j_1,j_2,j_3} + I^{m;-m,m,m}_{j;j_1,j_2,j_3} \tag{4.6a}$$

and

$$L^{(m)}_{j;j_1,j_2,j_3,j_4,j_5} \equiv 2J^{m;m,-m,-m,m,m}_{j;j_1,j_2,j_3,j_4,j_5} + 4\left(J^{m;-m,-m,m,m,m}_{j;j_1,j_2,j_3,j_4,j_5} + J^{m;m,-m,m,-m,m}_{j;j_1,j_2,j_3,j_4,j_5}\right). \tag{4.6b}$$

A. $b>0, d=0$

We first examine the behavior when only the leading-order nonlinearity is retained. In this case, it is easy to see that the elastic energy has a single minimum corresponding to $\nabla\eta_z(\mathbf{r},t)=\mathbf{0}$, i.e., an unstrained crystal. In addition, the cubic nonlinearity will cut off the exponential growth of the displacement field in the unstable regions.

Note that Eq. (4.5) forms a set of coupled damped-Mathieu-Duffing equations. The Duffing oscillator is a classic example of a nonlinear system where the oscilla-

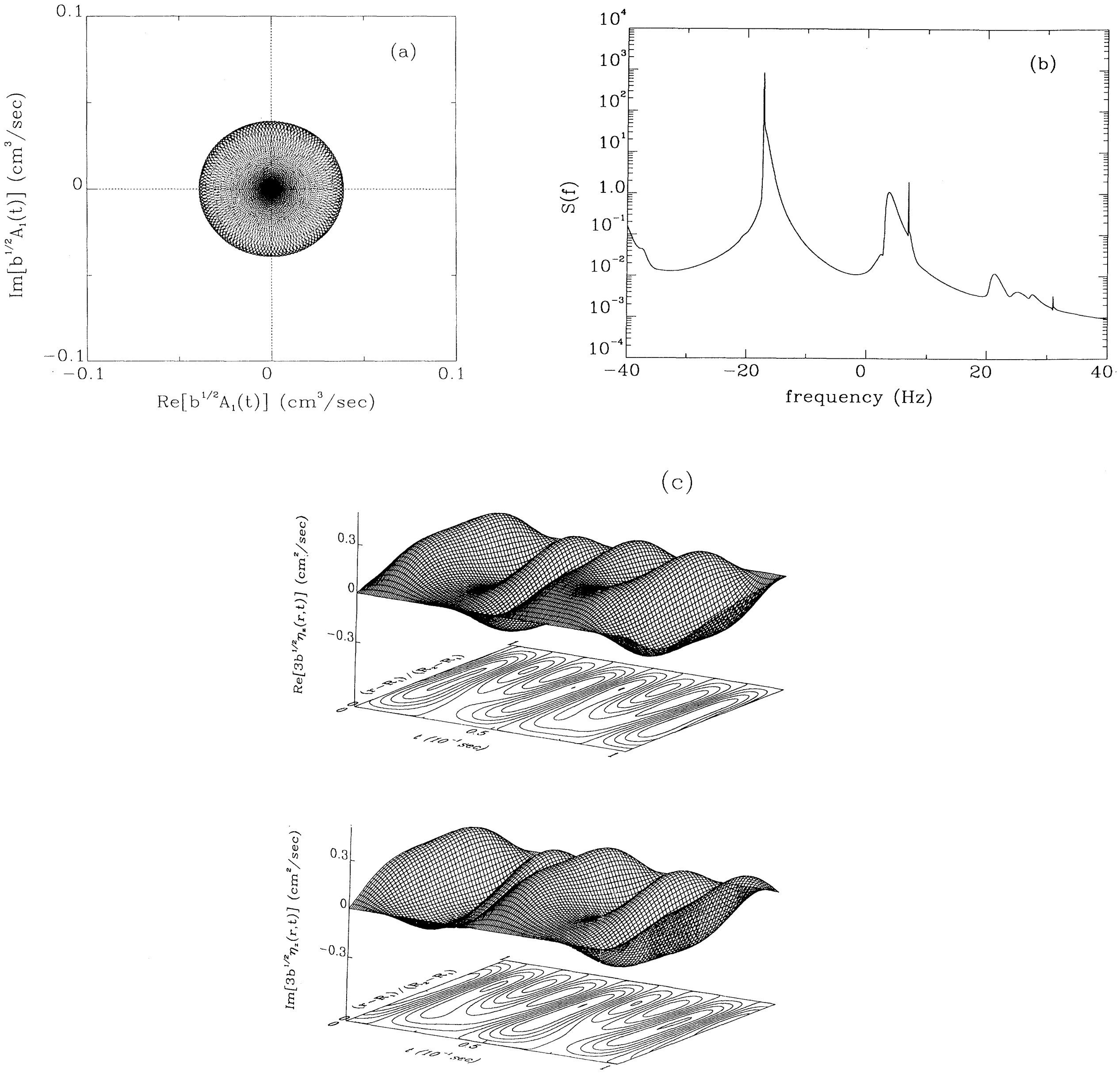

FIG. 10. (a) A phase portrait of the largest amplitude obtained by solving the four-mode equations inside a Mathieu unstable region for $m=36$, $c=10$ cm/sec, $\epsilon=0.05$, $\Omega_1=10.6\ \mathrm{sec}^{-1}$, $\Omega_2=0$, $b>0$, and $d=0$. The figure shows an 8-sec time range, starting at 12 sec. (b) The power spectrum of the solution to the nonlinear equations for the case shown in (a). The power spectrum is defined by Eq. (4.7), with $T=20$ sec. (c) The complex displacement field $\eta_z(\mathbf{r},t)$ for the cases shown in (a) and (b).

tion frequency becomes amplitude dependent [14]. This is especially interesting here since the instability is driven by resonances which require that the oscillator and modulation frequencies be related; cf. Sec. III. If the amplitude grows sufficiently large, the system will behave more like a Duffing oscillator, with concomitant changes in the natural oscillator frequency.

The truncated equations of motion, i.e., Eq. (4.6), were solved numerically; as mentioned above, the exponential growth in the unstable regions saturates and the amplitude of the displacement remains finite with $|\nabla\eta_z| \sim O(c/\sqrt{b}\,)$. A phase portrait for the largest amplitude in the time range where all the amplitudes have stopped growing exponentially is shown in Fig. 10(a). We define a power spectrum for the solutions as

$$S(f) \equiv \sum_{j=1}^{N} \left| \int_0^T \frac{dt}{T} A_j(t) e^{-i2\pi f t} \right|^2 , \tag{4.7}$$

where T is the time interval scanned. This power spectrum is shown in Fig. 10(b). Note that the components with positive frequency correspond to rotation opposite to Ω_1.

As long as the relative amplitudes are comparable, the components of the striped pattern with the slowest rotation rates should be easiest to perceive, and for the data shown in Fig. 10(b), these rotate at rates of 3.7 and 6.9 Hz in a direction opposite to inner cylinder rotation, with the latter having the larger amplitude. As the Ω_1 is increased, the faster, larger component speeds up, while the slower, smaller one slows down. Specifically, if the velocities of the associated components at $R = R_2$ are calculated, we find that $\mathrm{v} \sim -2.53\Omega_1 + 23.9$ (cm/sec) for the former, while $\mathrm{v} \sim 1.03\Omega_1 - 0.94$ (cm/sec), when Ω_1 is given in Hz. The behavior of the larger amplitude component is in the range reported in Ref. [2], although note that the experiment covers a much larger range of Ω_1 and it is fairly clear that the single-m approximation will break down (see below) in this range.

Finally, the displacement field can be reconstructed using Eq. (4.2), and an example of $\eta(\mathbf{r},t)$ within a Mathieu instability is presented in Fig. 10(c). Note the similarity between the displacement field obtained from the nonlinear equations and that characterizing the marginal state; cf. Figs. 10(c) and 5, respectively.

B. $b < 0, d > 0$

The stripes should vanish when the cylinder rotation is stopped for the cases shown in the preceding subsection, assuming that the one m-mode approximation is adequate. However, according to Ref. [4], this need not be the case, and the stripes can persist even after the rotation is stopped. One way to explain this observation is to introduce a metastable minimum into the elastic energy, specifically, one corresponding to a strained state.

An additional minimum in the elastic energy can occur when $b < 0$, although in this case, it is essential that the next nonvanishing terms in the expansion of the elastic energy [i.e., those proportional to d in Eq. (4.1)] have positive coefficients. It is easy to see that a second minimum in the elastic energy will occur when $|\nabla\eta_z| = \sqrt{[-b + (b^2 - 4dc^2)^{1/2}]/2d}$ if $b < -2cd^{1/2}$. Of course, we do not expect that this is the global minimum and hence we require that

$$1 < \frac{|b|}{2cd^{1/2}} < \frac{2}{\sqrt{3}} . \tag{4.8}$$

Some numerical examples are shown in Figs. 11(a)–11(d). Note that the solutions depend on the initial amplitude and two types of behavior were observed for the parameters used in the figures.

Examples of the behavior obtained with small initial amplitude are shown in Figs. 11(a) and 11(b). Most of the

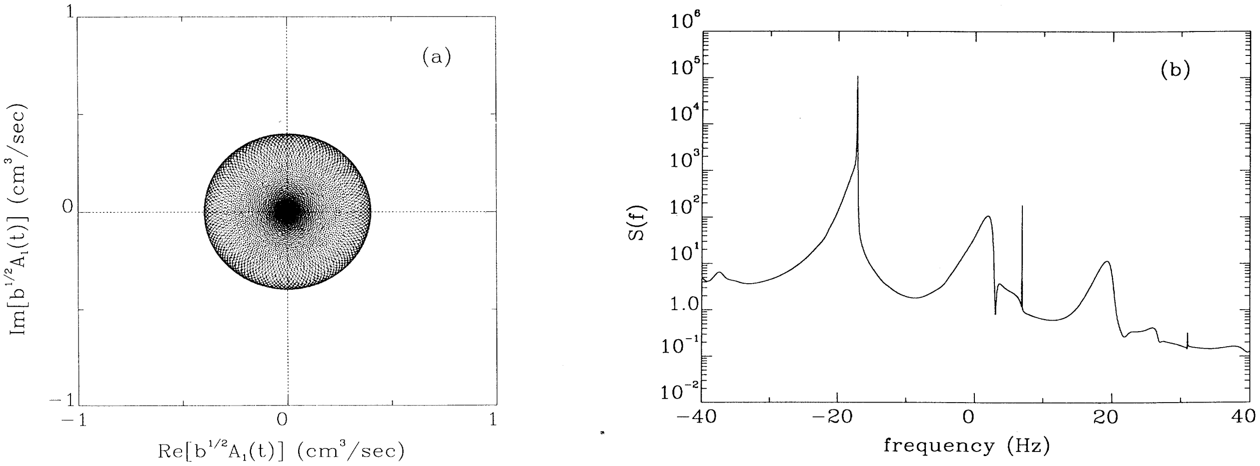

FIG. 11. (a) A phase portrait of the largest component obtained for small initial amplitudes in a Mathieu unstable region. Here $m = 36$, $c = 10$ cm/sec, $\epsilon = 0.05$, $\Omega_1 = 10.6$ sec^{-1}, $\Omega_2 = 0$, $b < 0$, and $d = 0.1876 b^2/c^2$. The number of amplitudes and time ranges is the same as in Figs. 10(a)–10(c). (b) The power spectrum of the solution used in (a). (c) A phase portrait for large initial amplitude for the parameters used in (a). (d) The power spectrum of the solution used in (c). (e) The displacement field for the case shown in (c) and (d).

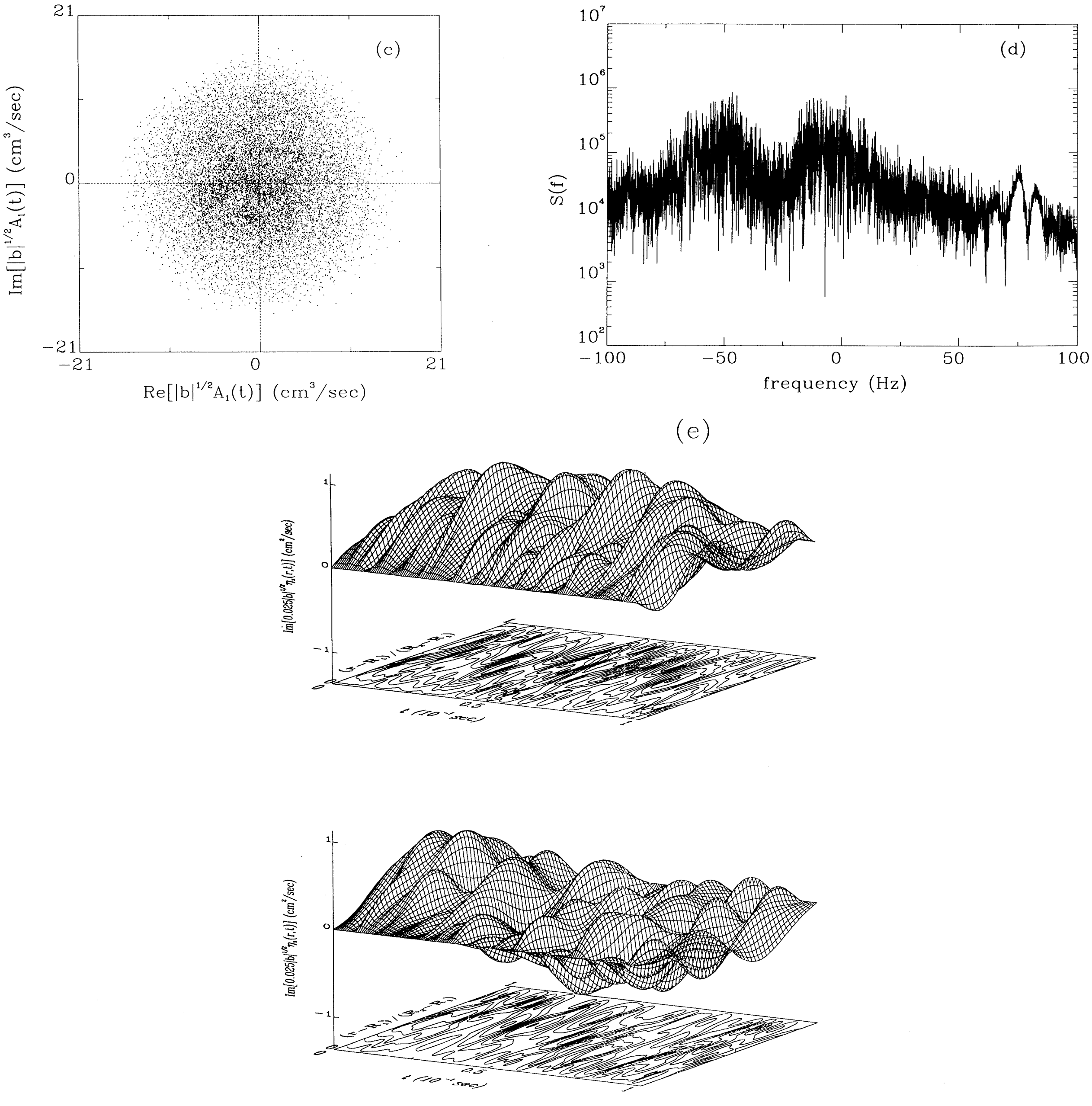

FIG. 11. (*Continued*).

features are similar to what was observed in Figs. 10(a)–10(c). The driving force associated with the Mathieu instability does not drive the amplitude over the barrier between the unstrained and strained configurations and the results shown in Figs. 11(a)–11(c) are not unexpected.

Very different behavior is obtained when the initial amplitude is large. An example is analyzed in Figs. 11(c)–11(e). Unlike the preceding cases, the motion is very irregular and the power spectrum is broad. In addition, unlike what was observed when $b > 0$, here there is a qualitative difference between the two-mode approximations and the higher-mode ones when the initial amplitude is large [15]. Quasiperiodic behavior is observed, even for large amplitude motion, if only two modes are kept, but this is an artifact of the approximation. Finally, we have carried out a limited study of the dependence of our results on the initial amplitudes and have only found the two types of behavior just described.

V. LIGHT-SCATTERING EXPERIMENTS

Many of the experiments on sheared colloidal crystals involve some form of light scattering. In this section, we examine what is measured in an ideal light-scattering experiment. It is well known that the scattered far-field intensity, resulting from elastic single scattering, and measured by heterodyne detection is proportional to

$$I \propto \int d\mathbf{k}_{\text{inc}}\, |E(\mathbf{k}_{\text{inc}})|^2 S_q(t), \tag{5.1}$$

where $|E(\mathbf{k}_{\text{inc}})|^2$ is proportional to the incident intensity at wave vector $\mathbf{k}_{\text{inc}}$,

$$S_q(t) \equiv \left\langle \sum_{i,j}{}' e^{i\mathbf{q}\cdot[\mathbf{r}_i(t)-\mathbf{r}_j(t)]} \right\rangle, \tag{5.2}$$

$\mathbf{q} \equiv \mathbf{k}_{\text{out}} - \mathbf{k}_{\text{inc}}$ is the momentum transfer for the scattering process, $|\mathbf{k}_{\text{out}}| = |\mathbf{k}_{\text{inc}}|$, and the prime on the sum in Eq. (5.2) implies that only particles within the illuminated volume should be considered. In writing Eq. (5.1) we have allowed for the possibility that the incident light may not be monochromatic or unidirectional. Finally, in what follows we assume that the illuminated region is large enough to include many colloid particles, but small compared to the characteristic length scales in $\boldsymbol{\eta}(\mathbf{r},t)$.

If η_z is slowly varying over the illuminated region, we can let

$$\mathbf{r}_j(t) - \mathbf{r}_k(t) \approx \{ 1 + \hat{\mathbf{z}}[\hat{\mathbf{r}} Q_r(\mathbf{R},t) + \hat{\boldsymbol{\phi}} Q_\phi(\mathbf{R},t)] \} \cdot \boldsymbol{\Delta}_{jk}(t), \tag{5.3}$$

where $\boldsymbol{\Delta}_{jk}(t) \equiv \mathbf{R}_j(t) - \mathbf{R}_k(t)$,

$$Q_r(\mathbf{R},t) \equiv \left[\frac{\partial \eta_z(\mathbf{r},t)}{\partial r} \right]_{\mathbf{r}=\mathbf{R}}, \tag{5.4a}$$

and

$$Q_\phi(\mathbf{R},t) \equiv \frac{1}{R} \left[\frac{\partial \eta_z(\mathbf{r},t)}{\partial \phi} \right]_{\mathbf{r}=\mathbf{R}}, \tag{5.4b}$$

where $\mathbf{R}$ denotes the center of the illuminated region.

It is easy to show that

$$\begin{aligned} \boldsymbol{\Delta}_{jk}(t) \sim{}& \boldsymbol{\nabla}_{\mathbf{R}}[e^{\Omega(R)\overleftrightarrow{T}t} \cdot \mathbf{R}] \cdot \boldsymbol{\Delta}_{jk}(0) \\ &+ O(\Delta_{jk}(0)[R_i(0) + R_j(0) - 2R]) \end{aligned} \tag{5.5}$$

within the illuminated region, where $\overleftrightarrow{T} \equiv \hat{\boldsymbol{\phi}}\hat{\mathbf{r}} - \hat{\mathbf{r}}\hat{\boldsymbol{\phi}}$ and $\Omega(R)$ is given by Eq. (2.4). Carrying out some simple algebra shows that

$$S_{\mathbf{q}} = \sum_{j,k} e^{i\mathbf{q}\cdot\overleftrightarrow{G}(\mathbf{R},t)\cdot\boldsymbol{\Delta}_{jk}(0)}, \tag{5.6}$$

where

$$\begin{aligned} \overleftrightarrow{\mathbf{G}}(\mathbf{R},t) \equiv{}& [1 + \hat{\mathbf{z}}\hat{\mathbf{r}} Q_r(\mathbf{R},t) \\ &+ \hat{\mathbf{z}}\hat{\boldsymbol{\phi}} Q_\phi(\mathbf{R},t)] \cdot e^{\Omega(R)\overleftrightarrow{T}t} \cdot [1 + \hat{\boldsymbol{\phi}}\hat{\mathbf{r}} R\,\Omega'(R)t]. \end{aligned} \tag{5.7}$$

Now, let $\{\boldsymbol{\Delta}_{jk}(0)\}$ form a Bravais lattice and $\mathbf{K}$ be a reciprocal lattice vector. The Bragg condition becomes

$$\overleftrightarrow{\mathbf{G}}^T(\mathbf{R},t) \cdot \mathbf{q} = \mathbf{K}. \tag{5.8}$$

We choose the local x-y-z axis to point along the r-ϕ-z directions, respectively. By using Eq. (5.7) in Eq. (5.8), we find that

$$\begin{bmatrix} q_x \\ q_y \\ q_z \end{bmatrix} = \begin{bmatrix} \cos\Omega t & -\sin\Omega t - R\,\Omega' t \cos\Omega t & -Q_r \\ \sin\Omega t & \cos\Omega t - R\,\Omega' t \sin\Omega t & -Q_\phi \\ 0 & 0 & 1 \end{bmatrix} \begin{bmatrix} K_x \\ K_y \\ K_z \end{bmatrix}. \tag{5.9}$$

This last expression simplifies when the measurement is done at the outer cylinder, which is also kept stationary. Since $\boldsymbol{\eta}(\mathbf{r},t) = 0$ for $r = R_2$, Q_ϕ vanishes, and Eq. (5.9) becomes

$$\begin{bmatrix} q_x \\ q_y \\ q_z \end{bmatrix} = \begin{bmatrix} 1 & -R\,\Omega' t & -Q_r \\ 0 & 1 & 0 \\ 0 & 0 & 1 \end{bmatrix} \begin{bmatrix} K_x \\ K_y \\ K_z \end{bmatrix}. \tag{5.10}$$

There are three contributions to the change in the scattering pattern; cf. Eq. (5.9). The first is simply rotation about the $\hat{\mathbf{z}}$ axis at rate $\Omega(R)$. The second results from the locally linear shear distortion of lattice and appears in the terms proportional to $R\,\Omega'(R)t$. Note that this results in a periodic distortion of the scattering pattern, where the period is roughly $[R\,\Omega'(R)]^{-1}$. Finally, there are the terms in $Q_{r,\phi}$. These are the only ones which are nonuniform in space and are responsible for the formation of the stripes.

Each of the foregoing contributions can be examined separately by choosing the direction of the momentum transfer. For example, the effect of the shear distortion of the lattice will not be seen if $K_y = 0$. Similarly, only the terms in the Q's will be seen if $q_x = q_y = 0$.

The observation of stripes is solely related to $Q_{r,\phi}(\mathbf{R},t)$. Some examples of $Q_{r,\phi}$ were computed using the nonlinear equations considered in Sec. IV, and their power spectra are shown in Figs. 12(a)–12(d). The spectra do not consist of a single frequency, and hence the observed pattern is a superposition of clockwise and counterclockwise rotating striped patterns, each rotating with angular velocity $-f/m$, and these should be measurable by spectrally analyzing the scattering data. (Strictly speaking, we should compute the structure factor and scattering intensity for a given experimental configuration in order to compare.)

If the system is viewed by eye, the slowest motion will be the one most easily perceived (assuming that the amplitudes are not too dissimilar), and for the data shown in Figs. 12(a)–12(d), this leads us to conclude that the stripes rotate in a direction opposite to the inner cylinder rotation, with angular velocity 1.2 sec^{-1} for $c = 10$ cm/sec, and $\epsilon = 0.05$ and 1.4 sec^{-1} for $c = 7$ cm/sec and $\epsilon = 0.06$, respectively. Of course, this conclusion is dependent on the relative magnitude of the slowest component being not too much smaller than the next slowest, etc., and this in turn depends on where the measurement is done; in general, the amplitude of the corotating component increases as R is moved to the inner cylinder. In reality, there are several slowly rotating components, and thus the analysis of the experiment is somewhat more complicated and will be considered in detail elsewhere.

It is interesting to note that order of magnitude of non-

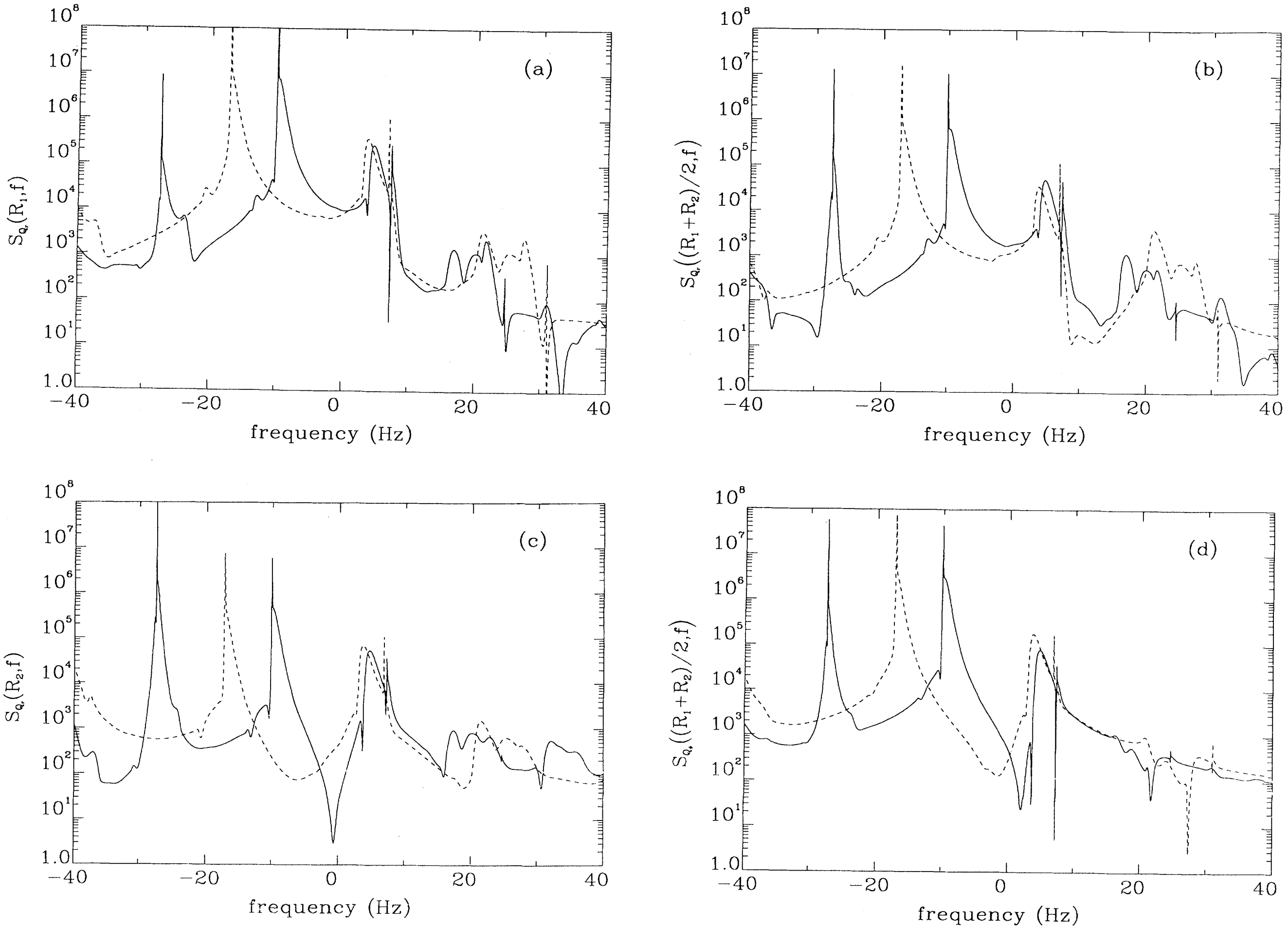

FIG. 12. (a) Power spectra for $Q_r(R,t)$ associated with the nonlinear solutions presented in Sec. IV A and evaluated at the inner cylinder. The solid curves are for $c=7$ cm/sec and $\epsilon=0.06$, while the dashed ones are for $c=10$ cm/sec and $\epsilon=0.05$. (b) Same as in (a), but now $R=(R_1+R_2)/2$. (c) Same as in (a), but now $R=R_2$, i.e., at the outer cylinder. (d) Same as in (b), but now the power spectra of $Q_\phi(R,t)$ are shown.

linear coefficients, i.e., b, d, etc. in Eq. (4.1), can be easily estimated. By using Eqs. (4.1), (4.2), and (5.10), we find that $b \sim O(c^2/|Q_r|^2)$ and $d \sim O(c^2/|Q_r|^4)$. In addition, by using reported color differences between adjacent stripes (red and green), it follows that $|Q_r| \sim 1/6$, which for $c=10$ cm/sec, implies that $b \sim 3600 cm^2/\mathrm{sec}^2$ and $d \sim O(10^5)$ cm^2/sec^2.

Finally, note that we have been purposely vague about specifying the lattice. The theory presented here is valid only for long-wavelength phenomena, and in particular we cannot preclude mechanisms which would lead to reconstruction of the lattice, either before or after the instabilities discussed here. Nonetheless, the instabilities discussed here must still occur, as long as the long wavelength properties can be discussed in terms of sheared elastic continua.

VI. DISCUSSION AND SUMMARY

In this work we have examined the long-wavelength behavior of sheared colloidal crystals in the Taylor-Couette geometry. We have shown that the usual Taylor instability is suppressed when the elasticity of the crystal is accounted for. Nonetheless, we have found two instability mechanisms that, unlike the Taylor instability, operate when either the inner or outer cylinder is rotated. Moreover, both of the instabilities result in modes with very different symmetry than the azimuthally symmetric Taylor rolls. The unstable modes consist of a large number of vertical stripes that are uniform in the vertical direction and that rotate in time. In addition, we have shown that the exchange-of-stability principle does not hold for the marginal states.

One of the instability mechanisms involves supersonic (in the sense that the tangential velocity difference across the gap between two cylinders is larger than twice the crystal transverse sound speed) flow in the crystal. The other is associated with the Mathieu instability and is analogous to the instability discussed in Ref. [4]. For an isotropic model for the elastic moduli, both instabilities have the displacement in the z direction. Moreover, of the two, the latter results in a pattern with a longer wavelength and exhibits many of the features reported in Ref. [2]. Note that, while the marginal state arises with a definite number of stripes, that number should slowly decrease as the shear rate increases (of course, this assumes that the symmetry of the nearest marginal state is reflected in the unstable one).

The behavior in the unstable regions was examined by deriving equations for the amplitudes; these were based on three key assumptions: (1) that the motion was uniform in the z; (2) that the symmetry of the marginal state (i.e., the direction of the displacement field and the number of stripes) dominates the unstable motion; and (3) the form of the colloidal crystal's elastic energy (here we considered two cases, i.e., those with a strained metastable minimum and those without). The second assumption is probably valid only near the onset of instability since range of unstable modes shifts to lower m as the rotation rate is increased. Nonetheless, this effect can be included in the theory presented in Sec. IV by including more m's in the equations of motion for the amplitudes; this will be investigated in the future.

While we have used a specific model for the dynamics of the colloid and the underlying fluid, several points must be stressed. First, much of the structure of the continuum equations, cf. Eqs. (2.7) and (2.8), could have been deduced without reference to an underlying microscopic model and the instabilities discussed here would still be obtained. An extreme example of this would arise if the shear of the colloidal lattice took place by having relatively large, but weakly aligned, domains of unsheared crystal slide over each other.

The continuum equations do not include more microscopic effects such as dislocations, and hence, if microscopic changes to the lattice occur, these will not be described in the current approximation. Nonetheless, the long-wavelength phenomena still takes place, even in the presence of dislocations, and the instabilities discussed in this work will occur. In molecular crystals, the energy required to have nondislocation mediated fracture is extremely high, and hence the required shear rates are very large. Since colloidal crystals are so soft, this does not seem to be the case here; the shear rates required to form a striped pattern are largely dependent on the system geometry and the transverse acoustic sound speed. The only adjustable parameter of the theory is ϵ in Eq. (A8). When experimental values are used, we have shown that the observed patterns occur in the right range of shear rates and have the right number of stripes and rotation speed.

Finally, we have ignored the space dependence of the local shear gradients in modeling the time-dependent transverse sound speed. As was discussed in the text, this is justified for thin samples. When this is not the case, then the modulation is not purely periodic and the effect on the instability, and in particular on the time dependence of the stripped pattern, is unclear. This point will be investigated in a future work.

ACKNOWLEDGMENTS

Portions of this work were supported by the Natural Sciences and Engineering Research Council of Canada and by Le Fonds pour la Formation de Chercheurs et l'Aide à la Recherche du Québec.

APPENDIX A

The colloidal force on ith particle is

$$\mathbf{f}(\mathbf{R}_i,t)=\sum_{j\,(\neq i)}\mathbf{F}(\mathbf{R}_{ij}+\boldsymbol{\eta}(\mathbf{R}_i,t)-\boldsymbol{\eta}(\mathbf{R}_j,t))-\mathbf{F}(\mathbf{R}_{ij}) \tag{A1}$$

$$\begin{aligned}&=\sum_{j\,(\neq i)}\mathbf{F}(\mathbf{R}_{ij}+\boldsymbol{\eta}(\mathbf{R}_i-\mathbf{R}_{ij}/2+\mathbf{R}_{ij}/2,t)\\&\qquad-\boldsymbol{\eta}(\mathbf{R}_i-\mathbf{R}_{ij}/2-\mathbf{R}_{ij}/2,t))-\mathbf{F}(\mathbf{R}_{ij}).\end{aligned} \tag{A2}$$

When viewed as a function of $\mathbf{R}_{ij}/2$ and $\mathbf{R}_i-\mathbf{R}_{ij}/2$,

$$\begin{aligned}&\mathbf{F}(\mathbf{R}_{ij}+\boldsymbol{\eta}(\mathbf{R}_i-\mathbf{R}_{ij}/2+\mathbf{R}_{ij}/2,t)\\&\quad-\boldsymbol{\eta}(\mathbf{R}_i-\mathbf{R}_{ij}/2-\mathbf{R}_{ij}/2,t))\end{aligned}$$

is narrowly peaked around $\mathbf{R}_{ij}=0$. The width of the peak is basically the force range a, which is microscopic, while L, the characteristic length scale upon which $\boldsymbol{\eta}(\mathbf{r},t)$ varies, is macroscopic, i.e.,

$$\frac{a}{L}\ll 1. \tag{A3}$$

Therefore, we may use the idea of Kramers and Moyal [9] to Taylor expand the $\mathbf{R}_i-\mathbf{R}_{ij}/2$ dependence of the force around $\mathbf{R}_{ij}/2=0$, i.e.,

$$\begin{aligned}\mathbf{f}(\mathbf{R}_i,t)=\sum_{n=1}^{\infty}\frac{1}{n!}\sum_{j\,(\neq i)}&\left[-\frac{\mathbf{R}_{ij}}{2}\cdot\frac{\partial}{\partial\mathbf{R}_i}\right]^n\\&\times\mathbf{F}(\mathbf{R}_{ij}+\boldsymbol{\eta}(\mathbf{R}_i+\mathbf{R}_{ij}/2)\\&\qquad-\boldsymbol{\eta}(\mathbf{R}_i-\mathbf{R}_{ij}/2)).\end{aligned} \tag{A4}$$

Here we have neglected $n=0$ term and the sum of all the $\mathbf{F}(\mathbf{R}_{ij})$ terms; they are zero as long as the sheared lattice has inversion symmetry locally. Clearly, this force is the spatial gradient of a tensor and thus momentum is conserved as expected. Furthermore, using Eq. (A3), we find that

$$\begin{aligned}\mathbf{f}(\mathbf{R}_i,t)=-\tfrac{1}{2}\sum_{j\,(\neq i)}\mathbf{R}_{ij}\cdot\frac{\partial}{\partial\mathbf{R}_i}&\mathbf{F}(\mathbf{R}_{ij}\cdot[\nabla\boldsymbol{\eta}(\mathbf{R}_i,t)+1])\\&+O(a/L),\end{aligned} \tag{A5}$$

and by keeping the leading order in a/L we obtain Eq. (2.9).

A formal expansion in powers of the strain-tensor $\nabla\boldsymbol{\eta}$ is easy to carry out. At the linear order, using Eq. (2.13), we find that

$$\mathbf{f}_1(\mathbf{r},t)=a\nabla^2\boldsymbol{\eta}(\mathbf{r},t), \tag{A6}$$

where the coefficient a is a real number and involves a lattice sum on the sheared lattice. In writing this last expression, we assume that the sheared lattice can be approximated as being locally isotropic; hence there is a single transverse sound speed.

For nonlinear terms, we restrict ourselves to the nonconvective instabilities discussed in Sec. III and consider only those terms important for the modes in the unstable regime. As was discussed in the text, these are η_z modes at $k_z=0$. The nth order nonlinear elastic contributions are denoted as $\mathbf{f}_n$, and have the form

$$\mathbf{f}_n=\hat{\mathbf{z}}\begin{cases}0 \text{ for } n \text{ even}\\ b_n\nabla\cdot[|\nabla\eta_z(\mathbf{r},t)|^{n-1}\nabla\eta_z(\mathbf{r},t)], \text{ for } n \text{ odd,}\end{cases} \tag{A7}$$

where b_n is real and again only involves a lattice sum. In general, the b_n's are periodic functions of time. However, for simplicity, we will model b_n as time independent for $n>1$, and include the simplest periodic modulation of the elastic properties in a, i.e., we assume that

$$\mathbf{f}_1(\mathbf{r},t)=\frac{\rho m_c c^2}{\rho_c}[1+2\epsilon\cos(\Gamma t)]\nabla^2\eta(\mathbf{r},t), \tag{A8}$$

where $c(1+2\epsilon)^{1/2}$ is the transverse sound speed the unsheared crystal, 2ϵ is the amplitude of the modulation caused by having planes of crystal sliding over each other, and Γ is the modulation frequency.

As discussed in Ref. [4], Γ is proportional to the local shear gradient. The proportionality constant depends on the lattice type and the orientation of the lattice with respect to the shear. For what follows, we assume that the proportionality constant is unity (e.g., as is the case for simple cubic lattices). In addition, for systems with a narrow gap between the cylinders, the shear gradient is roughly constant in space and we approximate Γ by the average velocity gradient.

APPENDIX B

Operators $\hat{A}$, $\hat{B}$, and $\hat{C}(t)$ in Eq. (3.1) can be written as 2×2 matrices with index 1(2) representing $r(\phi)$ component of $\vec{\eta}$. From Eqs. (2.16) and (2.17), we have

$$\hat{A}_{11}=k_z^2-D_r^-D_r^+, \tag{B1}$$

$$\hat{A}_{12}=-D_r^-\frac{im}{r}, \tag{B2}$$

$$\hat{A}_{21}=-\frac{im}{r}D_r^+, \tag{B3}$$

$$\hat{A}_{22}=k_z^2+\frac{m^2}{r^2}, \tag{B4}$$

$$\hat{B}_{11}=k_z^2\left[2im\Omega-\nu\left[\Delta-\frac{1}{r^2}\right]\right]-D_r^-(2im\Omega-\nu\Delta)D_r^+, \tag{B5}$$

$$\hat{B}_{12}=-2k_z^2\left[\Omega-\frac{im\nu}{r^2}\right]-D_r^-(2im\Omega-\nu\Delta)\frac{im}{r}, \tag{B6}$$

$$\hat{B}_{21}=2k_z^2\left[\Omega-\frac{im\nu}{r^2}\right]-\frac{im}{r}(2im\Omega-\nu\Delta)D_r^+, \tag{B7}$$

$$\hat{B}_{22}=k_z^2\left[2im\Omega-\nu\left[\Delta-\frac{1}{r^2}\right]\right]-\frac{im}{r}(2im\Omega-\nu\Delta)\frac{im}{r}, \tag{B8}$$

$$\hat{C}(t)_{ij}=\hat{G}_{ij}+c(t)^2\hat{H}_{ij}, \tag{B9}$$

where i and j run from 1 to 2 and

$$\hat{H}_{11}=-k_z^2\left[\Delta-\frac{1}{r^2}\right]+D_r^-\Delta D_r^+, \tag{B10}$$

$$\hat{H}_{12}=\frac{2imk_z^2}{r^2}+D_r^-\Delta\frac{im}{r}, \tag{B11}$$

$$\hat{H}_{21}=-\frac{2imk_z^2}{r^2}+\frac{im}{r}\Delta D_r^+, \tag{B12}$$

$$\hat{H}_{22}=-k_z^2\left[\Delta-\frac{1}{r^2}\right]+\frac{im}{r}\Delta\frac{im}{r}, \tag{B13}$$

$$\hat{G}_{11}=k_z^2\left\{\left[im\Omega-\nu\left[\Delta-\frac{1}{r^2}\right]\right]im\Omega+2r\Omega'\left[\Omega-\frac{im\nu}{r^2}\right]\right\}+D_r^-(\nu\Delta-im\Omega)im\Omega D_r^+, \tag{B14}$$

$$\hat{G}_{12}=-2im\Omega k_z^2\left[\Omega-\frac{im\nu}{r^2}\right]+D_r^-(\nu\Delta-im\Omega)\frac{m^2\Omega}{r}, \tag{B15}$$

$$\hat{G}_{21}=k_z^2\left[2im\Omega\left[\Omega-\frac{im\nu}{r^2}\right]+\nu\left[\Delta-\frac{1}{r^2}\right]r\Omega'\right]+\frac{im}{r}(\nu\Delta-im\Omega)im\Omega D_r^+, \tag{B16}$$

$$\hat{G}_{22}=imk_z^2\left[im\Omega-\nu\left[\Delta-\frac{1}{r^2}\right]\right]\Omega-\frac{im^3}{r}(\nu\Delta-im\Omega)\frac{\Omega}{r}. \tag{B17}$$

---

*Present address: IORL Research Center, 3535 Research Rd. N.W., Calgary, Alberta, Canada T2L 2K6.

[1] See, e.g., P. M. Chaikin, J. M. di Meglio, W. D. Dozier, and H. M. Lindsay, in *Physics of Complex and Super-Molecular Fluids*, edited by S. A. Safran and N. A. Clark (Wiley, New York, 1987).

[2] D. A. Weitz, W. D. Dozier, and P. M. Chaikin, J. Phys. (Paris) Colloq. **46**, C3-257 (1985).

[3] B. J. Ackerson and N. A. Clark, Physica (Utrecht) **118A**, 221 (1983); also see B. J. Ackerson, in *Physics of Complex and SuperMolecular Fluids* (Ref. [1]), p. 553.

[4] D. Ronis and S. Khan, Phys. Rev. A **41**, 6813 (1990).

[5] S. Ramaswamy and S. R. Renn, Phys. Rev. Lett. **56**, 945 (1986); B. Bagchi and D. Thirumalai, Phys. Rev. A **37**, 2530 (1988); P. Harrowell and M. Fixman, J. Chem. Phys. **87**, 4154 (1987). The first two of these theories use quasithermodynamic arguments, while the third is based on the Smoluchowski equation and the Lindemann melt-

ing criterion.

[6] S. Chandrasekhar, *Hydrodynamic and Hydromagnetic Stability* (Dover, New York, 1981).

[7] See, e.g., Ashcroft and Mermin, *Solid State Physics* (Holt, Rinehart and Winston, New York, 1976), Chap. 30.

[8] B. U. Felderhof and R. B. Jones, Z. Phys. B **64**, 393 (1986); Faraday Discuss. Chem. Soc. **83**, 69 (1987).

[9] N. G. van Kampen, *Stochastic Processes in Physics and Chemistry* (North Holland, Amsterdam, 1987).

[10] Strictly speaking, we only require that $\partial\eta_r(\mathbf{r},t)/\partial r$ vanish at the walls. The other components can have nonzero slope, and hence the basis functions for these components need not have vanishing derivatives.

[11] N. W. McLachlan, *Theory and Application of Mathieu Functions* (Dover, New York, 1964).

[12] E. T. Whittaker and G. N. Watson, *A Course of Modern Analysis* (Cambridge University Press, Cambridge, 1973), Chap. XIX.

[13] Remember that the imaginary parts of the Floquet exponents are defined modulo $n\Gamma$, where n is an integer. Here we chose the value which best describes the temporal oscillations in the marginal $\eta_z(\mathbf{r},t)$.

[14] See, e.g., C. M. Bender and S. A. Orszag, *Advanced Mathematical Methods for Scientists and Engineers* (McGraw-Hill, New York, 1978), Chap. 11.

[15] Note that in all the cases we have considered, the values obtained for the critical rotation speeds are not very accurate when only two amplitudes are retained. Nonetheless, the qualitative features of the numerical solutions have many features in common for $b > 0$ or for small initial amplitudes.